The Report Committee for Rodolfo Araujo Victor

Certifies that this is the approved version of the following report:

Pore Scale Modeling of Rock Transport Properties

APPROVED BY
SUPERVISING COMMITTEE:

Supervisor: _____
Maša Prodanović

_____
Steven L. Bryant

Pore Scale Modeling of Rock Transport Properties

by

Rodolfo Araujo Victor, B.S; M.S.

Report

Presented to the Faculty of the Graduate School of

The University of Texas at Austin

in Partial Fulfillment

of the Requirements

for the Degree of

Master of Science in Engineering

The University of Texas at Austin

August 2014

Dedication

To my dear wife and children.

Acknowledgments

I would like to thank my advisers, Dr. Maša Prodanović and Dr. Steven L. Bryant, for the guidance and encouragement throughout the evolution of my research. It was a real privilege to be able to learn from their experience during the time spent on discussions.

I am thankful to Petrobras for funding my education and providing the samples I needed to complete this part of the research. One special acknowledgment to Dr. Rodrigo Surmas from Petrobras Research Center, who helped me to collect the datasets. I also thank my brazilian manager and co-workers who have always encouraged me on this project.

To all my friends at UT, specially Elton Luiz Diniz Ferreira and Jose Sergio Cavalcanti, for the incredible amount of time spent together in and out class.

Finally, very special thanks for my dear wife Maria Carolina, and my dear children Joao Pedro, Francisco, Mariana, and Rafael, for being supportive and for understanding the many hours I needed to complete this work. I could not have done it without them.

Abstract

Pore Scale Modeling of Rock Transport Properties

Rodolfo Araujo Victor, M.S.E.
The University of Texas at Austin, 2014

Supervisor: Maša Prodanović

The increasing complexity of oil and gas reservoirs has led to the need of a better understanding of the processes governing the rock properties. Traditional theoretical and empirical models often fail to predict the behavior of carbonates, tight gas sands and shale gas, for example. An essential part of the necessary investigation is the study of the phenomena occurring at the pore scale. In this direction, the so-called digital rock physics is emerging as a research field that offers the possibility of imaging the rock pore space and simulating the processes therein directly. This report describes our work on developing algorithms to simulate viscous and electric flow through a three dimensional Cartesian representation of the porous space, such as those available through X-ray microtomography. We use finite differences to discretize the governing equations and also propose a new method to enforce the incompressible flow constraint under natural boundary conditions. Parallel computational codes are written targeting performance and computer memory optimization, allowing the use of bigger and more representative samples. Results are reported with an estimate of the error bars in order to help on the simulation appraisal. Tests performed using benchmark samples show good agreement with experimental/theoretical

values. Example of application on digital modeling of cement growth and on multiphase fluid distribution are also provided. The final test is done on Bentheimer, Buff Berea and Idaho Brown sandstone samples with available laboratory measurements. Some limitations need to be investigated in future work. First, the computer potential fields show anomalous border effects at the open boundaries. Second, a minor problem arises with the decreased convergence rate for the velocity field due to the increased number of operations, leading to the need of a more sophisticated preconditioner. We intend to expand the algorithms to handle microporosity (e.g. carbonates) and multiphase fluid flow.

Keywords: Pore scale modeling, finite difference simulation

Table of Contents

List of Figures

List of Tables

Chapter 1: Introduction

1.1 Motivation and objectives

The determination and prediction of porous rocks' macroscopic properties are an essential part in the work flow of oil and gas industry, from exploration geophysics and formation evaluation to reservoir and production engineering. Due to the lack of rigorous relations between the rock pore space and the corresponding petrophysical behavior, methods for predicting rock's responses to external stimulation have strongly relied on empirical correlations, whose fitting parameters are adjusted for a particular rock type using laboratory measurements. Two famous representatives of these correlations are the Archie's equation [1], relating rock electrical conductivity to water saturation, and the widely used power laws relating porosity and permeability (see, for example, Peters [2], chapter 3). The use of empirical methods, although somewhat successful when targeting the right set of rocks, often does not provide any insight on the fundamental physical principles relating the pore geometry and the macroscopic behavior of the rock.

Over the past decades, many approximate methods were proposed by representing rocks using idealized models such as bundle of capillary tubes or disordered pack of spheres [3–5]. Although these systems are much simpler than the actual porous media, the resulting equations showed a good performance in predicting physical properties of simpler rocks like clean sandstones [6]. However, general relations for complex rocks like carbonates and unconventional hydrocarbon reservoirs are a formidable task still to be completed.

In this context, a new approach known as *digital rock physics* [7, 8] has rapidly emerged as an outstanding technique to investigate processes at pore-level scale. Using modern experimental methods to acquire high resolution 3D images of rock samples, a

detailed model of the complex pore geometry is constructed and several physical processes with different scenarios can then be simulated and studied. This approach not only allows to estimate the bulk rock properties but also provides valuable insights towards a fundamental understanding of the governing pore-scale processes.

The objective of the present project is to develop and test algorithms to calculate electrical conductivity and absolute permeability in digital three dimensional rock images. We base the simulations on the fundamental physical principles governing each phenomenon. The algorithms use the finite difference technique, a well established discretization method that has been used by other authors to investigate pore scale processes. In addition, we propose a new method to enforce the pertinent physical constraints. Equally important, our decision to build a new suite of routines allows us to target computational and memory performance in the process, leading to the possibility of investigating larger and more representative samples with the same computational resources. Also, we avoid all the interpretation problems that usually arise when using "black box" software.

Validation of the results uses benchmark samples, whose properties are either theoretically known or measured in laboratory. We further exemplify the use of the methods to investigate cementation, relative permeability and resistivity index, and to characterize a set of sandstone samples from the original microtomographic images.

This chapter will continue with pertinent definitions and a literature review on the subject. Chapter 2 exposes the methodology in building the computational codes and also details the samples used to validate the method. Chapter 3 presents and discusses the results. Finally, chapter 4 lists conclusions and plans for future work.

1.2 Single-phase incompressible fluid flow through porous medium

1.2.1 Governing equations

The velocity field for a single-phase fluid is governed by two equations of change [9]. First, mass conservation leads to the equation of continuity,

$$\frac{\partial \rho}{\partial t} + \vec{\nabla} \cdot \rho \vec{v} = 0, \tag{1.1}$$

where $\rho(x, y, z, t)$ is the fluid density and $\vec{v}(x, y, z, t)$ is the fluid velocity. Our simulations will consider incompressible flow (ρ constant), what reduces the equation of continuity to

$$\boxed{\vec{\nabla} \cdot \vec{v} = 0}. \tag{1.2}$$

The equation of motion is constructed by writing the momentum balance over a volume element in the fluid. For a Newtonian fluid with viscosity μ and constant density ρ, this procedure leads to the Navier-Stokes equation

$$\rho \frac{D}{Dt} \vec{v} = -\vec{\nabla} p + \mu \nabla^2 \vec{v} + \rho \vec{g}, \tag{1.3}$$

where $D/Dt = \partial/\partial t + \vec{v} \cdot \vec{\nabla}$ is the material derivative, $p(x, y, z, t)$ is the fluid pressure and $\vec{g}$ is the gravitational acceleration. Pressure and gravity terms in the above equation can be conveniently lumped together as the so called modified pressure

$$\mathscr{P} = p + \rho g h, \tag{1.4}$$

where h is the distance measured in a direction opposite to gravity from some reference

point. In this notation, Navier-Stokes equation is written as

$$\rho \frac{D}{Dt}\vec{v} = -\vec{\nabla}\mathscr{P} + \mu\nabla^2\vec{v}. \tag{1.5}$$

We will indistinctly refer to $\mathscr{P}$ as pressure.

Flow regimes obeying equations (1.2) and (1.5) are characterized by a dimensionless group called Reynolds number

$$\text{Re} = \frac{l_0 v_0 \rho}{\mu}, \tag{1.6}$$

where l_0 and v_0 are respectively values of length and velocity characteristic of the flow regime. Flow regimes change from laminar at low Reynolds numbers to highly turbulent as this number increases.

Due to the small length scales involved in flow through a porous medium, incompressible flow regimes are usually in the low velocity laminar steady state, which can be accurately described by the Stokes equation

$$\boxed{\nabla^2\vec{v} = \frac{1}{\mu}\vec{\nabla}\mathscr{P}}, \tag{1.7}$$

obtained by neglecting the material derivative in equation (1.5). Equation (1.7) is also called the *creeping flow equation*.

The pressure field can be decoupled from equation (1.7) by the following procedure. First, take the divergence of that equation,

$$\vec{\nabla}\cdot\left(\mu\nabla^2\vec{v}\right) = \nabla^2\mathscr{P}, \tag{1.8}$$

and apply the vector identity

$$\vec{\nabla} \times \vec{\nabla} \times \vec{v} = \vec{\nabla}(\vec{\nabla} \cdot \vec{v}) - \nabla^2 \vec{v} \tag{1.9}$$

to obtain

$$\mu \vec{\nabla} \cdot \left(\vec{\nabla}(\vec{\nabla} \cdot \vec{v}) - \vec{\nabla} \times \vec{\nabla} \times \vec{v} \right) = \nabla^2 \mathscr{P}. \tag{1.10}$$

Since $\vec{\nabla} \cdot \vec{v} = 0$ from equation (1.2) and the divergence of a rotational is identically zero, we get a Laplace equation for the pressure field in the laminar regime:

$$\boxed{\nabla^2 \mathscr{P} = 0}. \tag{1.11}$$

1.2.2 Boundary conditions

The pressure and velocity fields for the flow inside the porous medium can be calculated from equations (1.2), (1.7), and (1.11) by defining the corresponding boundary conditions. Given an xyz coordinate system, we assume the flow can enter and exit the porous medium only through the first and last xy planes, driving the macroscopic flow in the z direction. No slip condition sets the tangent component of fluid velocity to zero at the pore-grain interface. No flux though the grain phase sets the normal component of velocity and the normal component of the pressure gradient also to zero at the pore-grain interface. Those are the most common used boundary conditions at solid walls [10, 11]. For the open boundaries, pressure is set to a constant value at both ends. We also assume no shear stress in the fluid outside the region defined by the porous medium, which results in zero normal derivatives for all the velocity components.

Let Ω be the region spanned by the pore space, $\partial\Omega$ be the pore-grain interface, Ω_{in} be the region composed by the open inlet pore voxels and Ω_{out} be the region composed by the open outlet pore voxels. Our fluid flow model is then described by the following

equations:

$$\begin{cases} \nabla^2 \mathscr{P} = 0 \\ \vec{\nabla} \cdot \vec{v} = 0 \\ \nabla^2 \vec{v} = \dfrac{1}{\mu} \vec{\nabla} \mathscr{P} \end{cases} \quad \text{in } \Omega, \tag{1.12}$$

$$\begin{cases} \mathscr{P} = \mathscr{P}_{in} \\ \dfrac{\partial v_x}{\partial z} = \dfrac{\partial v_y}{\partial z} = \dfrac{\partial v_z}{\partial z} = 0 \end{cases} \quad \text{in } \Omega_{in}, \tag{1.13}$$

$$\begin{cases} \mathscr{P} = \mathscr{P}_{out} \\ \dfrac{\partial v_x}{\partial z} = \dfrac{\partial v_y}{\partial z} = \dfrac{\partial v_z}{\partial z} = 0 \end{cases} \quad \text{in } \Omega_{out}, \tag{1.14}$$

$$\begin{cases} \vec{\nabla} \mathscr{P} \cdot \hat{n} = 0 \\ v_x = v_y = v_z = 0 \end{cases} \quad \text{at } \partial\Omega. \tag{1.15}$$

1.2.3 Effective medium property: the absolute permeability

Solution of Navier-Stokes equation gives detailed information about the fluid velocity at the pore scale. A more practical description for oil industry is the concept of permeability introduced by Darcy[1] in 1856, in an experimental work on water flow through a sand pack. He observed that the volumetric flow rate q through a specific porous medium is linearly proportional to the difference between the inlet and the outlet pressures. These quantities are related by the Darcy's law

$$q = \frac{\kappa A}{\mu} \frac{\Delta p}{L}, \tag{1.16}$$

where A is the area of a cross-section perpendicular to the flow direction, L is the length of the sample and κ is the porous medium property called *absolute permeability*. For inclined flow forming an angle α with the horizontal, gravity can be included in Darcy's law using

[1] English translation of Darcy's original work is available on
`http://biosystems.okstate.edu/darcy/index.htm`

the modified pressure:

$$q = \frac{\kappa A}{\mu L}(\Delta p + \rho g h \sin\alpha) = \frac{\kappa A}{\mu L}(\Delta p + \rho g \Delta h), = \frac{\kappa A}{\mu}\frac{\Delta \mathscr{P}}{L}. \tag{1.17}$$

Later, Whitaker [12] showed that volumetric averages on incompressible creeping flow of single-phase fluid in a porous medium lead to Darcy's law. Thus, velocity field from Stokes equation and volumetric flow rate from Darcy's law are linked by

$$q = \oint \vec{v} \cdot \hat{n} dA, \tag{1.18}$$

with the integral taken over a cross-section perpendicular to the flow direction.

Absolute permeability is a geometric property describing the ability of the pore space to conduct the flow. Its common unit is the darcy (D), which is approximately equal to 10^{-12} m^2. For a 3D flow in an anisotropic medium, Darcy's law is generalized to

$$\vec{q} = -\frac{1}{\mu}\bar{\bar{\kappa}} : \vec{\nabla}\mathscr{P}, \tag{1.19}$$

where $\bar{\bar{\kappa}}$ is a second order tensor called the *permeability tensor*. More details can be found in Peters [2].

1.3 Multiphase fluid flow in porous medium

1.3.1 Interfacial tension and wettability

Two immiscible fluids in contact generate a curved interface due to the larger attractive forces between molecules in the same phase than the ones between molecules in distinct phases. The interfacial tension is a thermodynamic property of the interface, and is defined as the energy required to increase the area of the interface by one unit [13]. Solid surfaces in contact with two immiscible fluids will attract each fluid phase with different in-

tensities. The phase more strongly attracted to the solid surface is called the *wetting phase*, while the other is the *non wetting phase*.

Wettability depends on the properties of solid surface and fluid phases. Some quantitative analysis is given by examining the force balance at the contact line between the two fluids and the solid surface. Figure 1.1 gives an example for a water wet surface in presence or a mixture of water and oil. Forces at the contact line are the solid-oil interfacial tension γ_{so}, the solid-water interfacial tension γ_{sw} and the oil-water interfacial tension γ_{ow}. At equilibrium, the sum of the three forces must be zero. The force balance in the direction parallel to the solid surface defines the Young equation

$$\gamma_{os} - \gamma_{ws} = \gamma_{ow} \cos\theta. \tag{1.20}$$

In general, γ_{os} and γ_{ws} are not known, making the contact angle θ the principal experimental measurement of wettability.

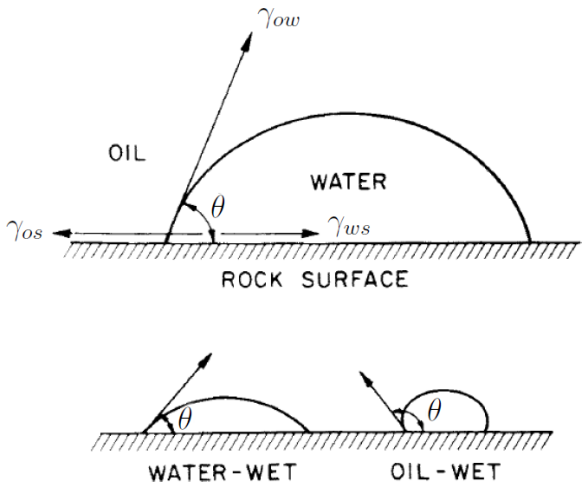

Figure 1.1: Wettability for a mixture of oil and water. Modified from Willhite [13].

1.3.2 Capillary pressure

In small regions such as in a rock porous space, wettability phenomenon causes a measurable pressure difference between the two fluid phases across the curved interface. This pressure difference is what is defined as the *capillary pressure* [2, 13],

$$p_c = p_{nw} - p_w, \tag{1.21}$$

where p_{nw} and p_w represent the pressure values for the non wetting and the wetting phases, respectively.

The equation for p_c in a capillary tube can be derived by balancing the four forces acting on the fluid (see Figure 1.2)

$$p_{nw}\pi r^2 - \gamma_{nws} 2\pi r = p_w \pi r^2 - \gamma_{ws} 2\pi r, \tag{1.22}$$

$$p_{nw} - p_w = \frac{2}{r}(\gamma_{ws} - \gamma_{nws}), \tag{1.23}$$

and by equations (1.20) and (1.21),

$$p_c = \frac{2\gamma_{nww}\cos\theta}{r}. \tag{1.24}$$

The above equation is a particular case of the Young-Laplace equation

$$p_c = 2C\gamma_{nww}, \tag{1.25}$$

where C is the local mean curvature of the interface. A thermodynamic based derivation of the Young-Laplace equation is given by Morrow [14].

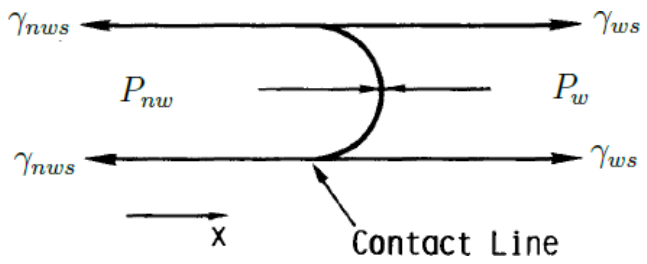

Figure 1.2: Two-phase fluid configuration in a capillary tube. Modified from Willhite [13].

1.3.3 Effective permeability in multiphase flow: the relative permeability

Effective permeabilities in a multiphase fluid flow through the porous medium are calculated by applying Darcy's law to each phase, as if the other phase did not exist. For a two-phase flow regime, the equations become

$$q_w = \frac{\kappa_w A}{\mu_w L}\Delta\mathscr{P}_w \quad \text{(wetting phase)}, \tag{1.26}$$

$$q_{nw} = \frac{\kappa_{nw} A}{\mu_{nw} L}\Delta\mathscr{P}_{nw} \quad \text{(non wetting phase)}. \tag{1.27}$$

Capillary pressure is given by

$$p_c = p_{nw} - p_w = \mathscr{P}_{nw} - \mathscr{P}_w. \tag{1.28}$$

Effective permeability is generally presented as relative permeability, usually defined as the ratio of the effective permeability to the absolute permeability κ of the medium:

$$\kappa_{r,w} = \frac{\kappa_w}{\kappa}, \tag{1.29}$$

$$\kappa_{r,nw} = \frac{\kappa_{nw}}{\kappa}. \tag{1.30}$$

The validity of the above equations assume the following conditions, based on experimental observations [13]:

- low Reynolds number, as required by Darcy's law;
- negligible viscous coupling between the two phases;
- both phases flow simultaneously at a constant overall rate;
- each phase flows under its own pressure gradient;
- each phase flows through its own network of interconnected, tortuous channels, in laminar flow regime.

1.4 Flow of electric current through porous medium

1.4.1 Governing equations

Let $\vec{E}(x, y, z)$ be an applied external electrostatic field and $\sigma(x, y, z)$ the electrical conductivity of the porous medium, both varying with position. The resulting electric current density $\vec{J}(x, y, z)$ is given by Ohm's law

$$\vec{J} = \sigma \vec{E}. \tag{1.31}$$

From continuity equation for electric flow,

$$\vec{\nabla} \cdot \vec{J} + \frac{\partial \zeta}{\partial t} = 0, \tag{1.32}$$

where ζ is the local charge density. Imposing charge conservation (no charge is created or destroyed), we get incompressible vector field $\vec{J}$,

$$\vec{\nabla} \cdot \vec{J} = \vec{\nabla} \cdot \left(\sigma \vec{E}\right) = 0. \tag{1.33}$$

Since the electrostatic field must be irrotational ($\vec{\nabla} \times \vec{E} = \vec{0}$), we can describe it using a scalar potential field φ,

$$\vec{E} = -\vec{\nabla}\varphi, \tag{1.34}$$

resulting in the generalized Laplace equation for this potential field

$$\boxed{\vec{\nabla} \cdot (\sigma \vec{\nabla}\varphi) = 0}. \tag{1.35}$$

Detailed description of classical electrodynamics is provided by Jackson [15]. The above equation reduces to an analogue of equation (1.11) if conductivity is constant through the porous medium. The varying electric conductivity will allow us to account for microporous voxels not resolved in μ-CT images in future work.

1.4.2 Boundary conditions

Similar to viscous fluid flow, the flow of electric current is directed to z direction by allowing electric flow in and out only at the external xy planes. Potential is fixed at the open flow boundaries and the normal component of the electric current density is set to zero at conducting–non conducting interfaces:

$$\vec{J} \cdot \hat{n} = (\sigma \vec{\nabla}\varphi) \cdot \hat{n} = \sigma \frac{\partial \varphi}{\partial n} = 0 \quad \Rightarrow \quad \frac{\partial \varphi}{\partial n} = 0. \tag{1.36}$$

The following equations summarize the electric flow model:

$$\vec{\nabla} \cdot (\sigma \vec{\nabla}\varphi) = 0 \qquad \text{in } \Omega, \tag{1.37}$$

$$\varphi = \varphi_{in} \qquad \text{in } \Omega_{in}, \tag{1.38}$$

$$\varphi = \varphi_{out} \qquad \text{in } \Omega_{out}, \tag{1.39}$$

$$\vec{\nabla}\varphi \cdot \hat{n} = 0 \qquad \text{at } \partial\Omega, \tag{1.40}$$

where Ω, Ω_{in}, Ω_{out} and $\partial\Omega$ are the analogues of the definitions in section 1.2.2, now for the electrically conducting space.

1.4.3 Effective medium property: the formation factor

Once the electric potential $\varphi(x, y, z)$ inside the porous medium is known, the total electrical current I through the rock can be calculated as

$$I = \oint \vec{J} \cdot \hat{n} dA, \tag{1.41}$$

where

$$\vec{J} = \sigma \vec{\nabla} \varphi. \tag{1.42}$$

The rock electrical conductivity is then given by

$$\sigma_{rock} = \frac{LI}{A\Delta V}, \tag{1.43}$$

where L is the sample length in z direction, A is the area of an xy slice and ΔV is the macroscopic electric potential difference applied in the rock extremes. For the 3D anisotropic flow, electrical current density is not necessarily parallel to the electric potential gradient, and Ohm's law in equation (1.42) generalizes to

$$\vec{J} = \bar{\bar{\sigma}} : \vec{\nabla} \varphi, \tag{1.44}$$

where the *conductivity tensor* $\bar{\bar{\sigma}}$ is a second order tensor describing how the electric flow is generated by the applied electric potential.

On investigating the correlation between the electrical resistivity of the formation and its character and saturating fluid, Archie [1] introduced the formation resistivity factor, or simply the formation factor F, as a measure of the enhancement of electrical resistivity

due to the porous medium. It is defined as the ratio of the electrical resistivity of a rock filled with water to the electrical resistivity of the water,

$$F = \frac{R_{rock}}{R_{water}}. \tag{1.45}$$

Since our simulations use the value of electrical current to measure the electrical conductivity, a more natural way to appraise the results is through the reciprocal of formation factor, what we will call the *normalized conductivity*

$$\hat{\sigma} = \frac{\sigma_{water}}{\sigma_{rock}}, \tag{1.46}$$

where σ_{water} and σ_{rock} are the electrical conductivities of the water and the rock filled with the water, respectively.

After collecting a number of results for consolidated and clean sandstone cores with non-conducting matrices and 100% saturated with brine, Archie proposed the empirical correlation

$$F = \phi^{-m}, \tag{1.47}$$

where ϕ is the total porosity. The exponent m, now called the *cementation exponent*, was found to be in the range between 1.8 and 2.0 for consolidated sandstones and about 1.3 for clean unconsolidated sands packed in the laboratory. Similar studies in the following years (see Kennedy and Herrick [16] for a review) introduced another fitting parameter, modifying equation (1.47) to

$$F = a\phi^{-m}. \tag{1.48}$$

The constant a is known as the tortuosity factor.

1.4.4 Electrical conductivity for multiphase fluid saturated rock: the resistivity index

The rock effective electrical conductivity will decrease if non conducting oil coexists with conducting brine in the pore space. In his seminal paper, Archie [1] also proposed an empirical correlation for the rock electrical resistivity and the water saturation S_w through the *resistivity index*

$$RI = \frac{R_t}{R_0} = S_w^{-n}, \tag{1.49}$$

where R_t is the electrical resistivity of the rock partially saturated with non conducting fluid, R_0 is the resistivity of the rock fully saturated with brine. The exponent n is called the *saturation exponent*. Archie's work found n close to 2 for clean sands at water saturations down to 0.15 or 0.20.

Considering these results, the formation water saturation, necessary for calculating hydrocarbon reserves, can be estimated as

$$S_w = \left[\frac{a}{\phi^m}\frac{R_{water}}{R_t}\right]^{\frac{1}{n}}. \tag{1.50}$$

This equation remains as the industry standard porosity-resistivity model. Yet, it is important to emphasize that it is an empirical correlation describing a trend for laboratory data for clean sandstones, plotted on log scale graph paper, the technology available at the time. Deviations from equation (1.49) have been observed even in clean siliciclastic rocks like the Fontainebleau sandstone, since ionic conduction can still be carried through the thin film of brine coating the water wet grains at low water saturations. Recent authors have investigated the influence of surface conduction on the rock effective conductivity [17–19]. Carbonate rocks are also well known deviations from equation (1.50) [20–24].

1.5 The state of art of digital petrophysics

The work flow in digital petrophysics is formed by three main steps. First, a 3D pore-scale image of the rock sample is acquired. The most used imaging technique is the X-ray computed micro-tomography (μ-CT), which measures the local X-ray absorption in a sample whose dimensions span a few millimeters. Using 2D radiographs acquired at different angles, a 3D gray scale image is reconstructed, with brightness proportional to the X-ray attenuation coefficient (and thus also proportional to the density of the material) at each spatial position in the sample. Flannery *et al.* [25] introduced the technique. Recent reviews are provided by Wildenschild and Sheppard [8], and Cnudde and Boone [26].

The second and probably most critical step is to classify each voxel as a mineral phase, a fluid phase or a combination of both if there is not enough resolution to make the distinction. This step, called *segmentation* is usually preceded by some pre-processing, with the objective to enhance the image quality before the segmentation algorithm takes place. Pre-processing usually includes noise filtering and removing of image artifacts. Image segmentation constitutes a non trivial research field and may require highly sophisticated methods when working with complex rocks. It is often subject to parameters that need to be decided manually for each sample, leading to non unique results and requiring quality control as a final step. Comprehensive reviews on the available segmentation methods are provided by the works of Iassonov *et al.* [27] and Schlüter *et al.* [28]. Figure 1.3 shows a simple example.

The final step is the pore space characterization and simulation of the physical processes within the segmented image. This step leads to an estimate of the rock's bulk behavior and its petrophysical properties, but also gives the opportunity to test different system configurations and validate theoretical models through comparison between simulation results and laboratory measurements.

One approach uses networking modeling to represent the pore space as a network of

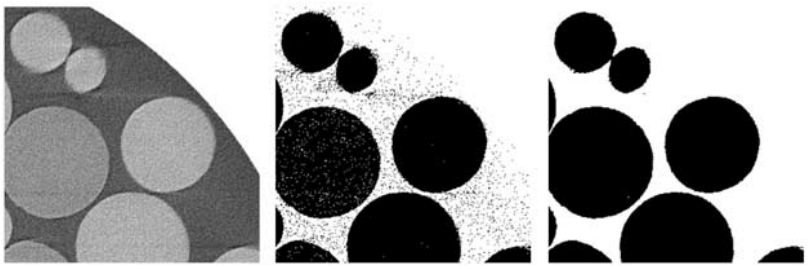

Figure 1.3: Example of image segmentation from Iassonov *et al.* [27]. Left: original noisy gray scale image. Center: binary version using manual thresholding. Right: binary version using indicator kriging. See the reference for details.

sites corresponding to pore bodies, connected by bonds corresponding to pore throats. An usual practice is to represent pore bodies by spheres and pore throats by cylinders. Macroscopic properties can then be simulated by applying the pertinent conservation equations describing the phenomenon of interest. Finney [3] experimentally measured the spatial position of approximately 8000 precision ball bearings in a dense random pack. Pore networks using Finney's data showed good performance in predicting transport properties for simple sandstones [6, 29, 30]. Modern modeling now starts from 3D images of rock samples. A review on this method is provided by Blunt *et al.* [31, 32]. Recent works have applied pore network modeling to investigate unconventional resources like tight-gas sandstones [33] and shale gas [34].

Network modeling, although computationally cheaper, simplifies the velocity field within the pore space. An intermediate solution is given by Shabro *et al.* [11], where the pore voxels are divided into interconnected cylindrical pores, each one with a flow described by the Hagen-Poiseuille equation. The overall flow rate is then achieved by weighting the mass flux in each cylinder using the distance from the cylinder to the nearest grain voxel.

In the last decade, increasing computational resources have made possible the application of direct simulation methods in 3D images. An established method to simulate single and multiphase fluid flow at pore scale in complex geometries is the lattice-Boltzmann

method [35, 36]. In this approach, the fluid is modeled by a collection of particles following simple rules for local interactions, recovering the Navier-Stokes equation for the macroscopic fluid behavior. The absolute permeability is then estimated by using Darcy's law after calculating the inlet and the outlet pressures. This method can provide a rigorous estimate of flow properties, since there is no additional simplification to the pore-space. Results for estimating absolute permeability using the lattice-Boltzmann method are widely available in the literature [22,37–39]. Two phase relative permeability estimated by lattice-Boltzmann has also been reported [40], but to date is still computationally expensive.

Another common method for permeability is to directly solve Stokes or Navier-Stokes equation using the method of finite differences. Yet, incompressible flow boundary conditions at open boundaries have been a point of discussion among different authors [10, 41–43]. One common approach is to specify a velocity profile at either the inlet or the outlet open boundary, but this can lead to artificial flow configurations at complex pore spaces. The boundary conditions discussed in section 1.2.2 are the closest to the real experiment set up, but also lead to non uniqueness and non zero divergence at the solution. Silin and Patzek [44] use the method of artificial compressibility in a staggered grid to achieve a zero divergence solution. We will present a different method in the next chapter. Finite volume method is another used technique to solve Navier-Stokes in the pore space [45].

The main methods to calculate formation factor are also finite differences [19] and finite elements [22, 23, 39, 46]. Andra [38] compares solution from these two methods with another called explicit jump averaging, whose details are found in [47]. Yue [48] uses lattice-Boltzmann for electrical conductivity simulation. Similar procedures for elastic moduli [38, 39, 49, 50] and nuclear magnetic resonance response [5, 51–54] have also been developed.

Accurate multiphase fluid distribution on the pore space is an important step on the

simulation of multiphase fluid properties. Three methods that handle fluid distribution on pore space are available in the literature. First, the method of maximal inscribed spheres [55] assigns to each voxel the radius of the maximal sphere included in the pore space and covering that voxel. Invasion scenarios are then created by cluster search on these radii map. This method is used by Silin and Patzek to calculate relative permeability [44].

Another similar method is called the capillary drainage transform [56]. This method simulates drainage by letting a non wetting phase invade a pore region if a sphere with radius given by equation (1.24) (page 9) can be moved from a non wetting saturated region tho the target region. Capillary drainage transform is used to calculate resistivity index in [23, 57, 58].

A more accurate method, called level set based progressive *quasi*-static algorithm (LSMPQS) is described in [59]. Level sets formulation is used to move the fluid-fluid interface through the porous medium, with Young-Laplace equation (1.25) enforced at each equilibrium position. LSMPQS successfully matches experimentally observed trapped non wetting phase [60–62].

Chapter 2: Methods and Samples

2.1 Finite difference approximation of governing equations

We chose the finite difference method [63] to discretize the equations governing the transport of fluid and electric charge. Finite differences has several advantages over other methods. First, it uses the segmented image without any further processing, since it is a 3D Cartesian grid representation of the original porous medium. Detailed representation for all quantities in the pore space is a natural consequence. In pore-network modeling, for example, generating a network reflecting the specific properties of an arbitrary porous medium is still a challenge.

Second, boundary conditions such as no-slip at pore-grain contact and fixed pressure at the open boundaries are straightforward to implement. A rigorous implementation of these conditions may not be as simple in lattice-Boltzmann simulation. Finally, a careful implementation of finite differences can lead to fast and relatively cheap algorithms. It can be a promising alternative, for example, for lattice-Boltzman simulations of two-phase flow with the interfacial phenomena, which so far still require massive computations.

The main disadvantage of finite differences with open flow boundary conditions is the residual divergence at the velocity field. We propose a new way to solve this problem as will be explained in the following sections.

2.1.1 Discretization of pressure field equation

Let n_x, n_y, and n_z be the number of voxels in x, y, and z directions, respectively, h_x, h_y, and h_z be the voxel size in each direction and i, j, and k be the corresponding voxel coordinates, such that $1 \leq x \leq n_x$, $1 \leq y \leq n_y$ and $1 \leq z \leq n_z$. For the sake of simplicity

in the notation, let us also introduce $n_{xy} = n_x n_y$ and $n_{xyz} = n_x n_y n_z$.

The second order central finite difference for the Laplace equation for pressure (equation (1.11)) for the voxel at position (i, j, k) is given by

$$\frac{\mathscr{P}_{i+1,j,k} - 2\mathscr{P}_{i,j,k} + \mathscr{P}_{i-1,j,k}}{h_x^2} + \frac{\mathscr{P}_{i,j+1,k} - 2\mathscr{P}_{i,j,k} + \mathscr{P}_{i,j-1,k}}{h_y^2} + \frac{\mathscr{P}_{i,j,k+1} - 2\mathscr{P}_{i,j,k} + \mathscr{P}_{i,j,k-1}}{h_z^2} = 0. \quad (2.1)$$

The set of the above equations for each voxel in the 3D grid forms a system of n_{xyz} equations and n_{xyz} variables. In order to use the formalism of matrix algebra, we introduce the index

$$\boxed{K = (k-1)n_{xy} + (j-1)n_x + i}, \quad (2.2)$$

to put the n_{xyz} equations in the form

$$\frac{1}{h_z^2}\mathscr{P}_{K+n_{xy}} + \frac{1}{h_y^2}\mathscr{P}_{K+n_x} + \frac{1}{h_x^2}\mathscr{P}_{K+1} - \left(\frac{2}{h_x^2} + \frac{2}{h_y^2} + \frac{2}{h_z^2}\right)\mathscr{P}_K + \frac{1}{h_x^2}\mathscr{P}_{K-1} + \frac{1}{h_y^2}\mathscr{P}_{K-n_x} + \frac{1}{h_z^2}\mathscr{P}_{K-n_{xy}} = 0. \quad (2.3)$$

To handle the Dirichlet boundary conditions, equation (2.3) has to be modified at $k = 1$ and $k = n_z$. If we define $\mathscr{P}_{in}$ and $\mathscr{P}_{out}$ to be the pressure values at the inlet and outlet open boundaries, respectively, the corresponding equations for voxels at $k = 1$ will be modified to

$$\frac{1}{h_z^2}\mathscr{P}_{K+n_{xy}} + \frac{1}{h_y^2}\mathscr{P}_{K+n_x} + \frac{1}{h_x^2}\mathscr{P}_{K+1} - \left(\frac{2}{h_x^2} + \frac{2}{h_y^2} + \frac{2}{h_z^2}\right)\mathscr{P}_K + \frac{1}{h_x^2}\mathscr{P}_{K-1} + \frac{1}{h_y^2}\mathscr{P}_{K-n_x} = -\frac{\mathscr{P}_{in}}{h_z^2}, \quad (2.4)$$

while equations for voxels at $k = n_z$ will become

$$\frac{1}{h_y^2}\mathscr{P}_{K+n_x} + \frac{1}{h_x^2}\mathscr{P}_{K+1} - \left(\frac{2}{h_x^2} + \frac{2}{h_y^2} + \frac{2}{h_z^2}\right)\mathscr{P}_K + \frac{1}{h_x^2}\mathscr{P}_{K-1} + \frac{1}{h_y^2}\mathscr{P}_{K-n_x} + \frac{1}{h_z^2}\mathscr{P}_{K-n_{xy}} = -\frac{\mathscr{P}_{out}}{h_z^2}. \quad (2.5)$$

Voxels with $i = 1$, $j = 1$, $i = n_x$, $j = n_y$ are set to grain phase to enforce closed boundaries. Implementation of zero normal derivative for pressure at grain-pore interface is also is also straightforward using central difference. For example, if the normal direction at pore-grain interface is parallel to $\hat{x} + \hat{y}$, we have

$$\frac{\partial \mathscr{P}}{\partial n} = \vec{\nabla}\mathscr{P} \cdot \hat{n} = \vec{\nabla}\mathscr{P} \cdot \left(\frac{\hat{x} + \hat{y}}{\sqrt{2}}\right) = 0 \quad (2.6)$$

and, by finite differences

$$\frac{\partial \mathscr{P}}{\partial x} + \frac{\partial \mathscr{P}}{\partial y} = 0, \quad (2.7)$$

$$\frac{\mathscr{P}_{K+1} - \mathscr{P}_{K-1}}{2h_x} + \frac{\mathscr{P}_{K+n_x} - \mathscr{P}_{K-n_x}}{2h_y} = 0, \quad (2.8)$$

which is enforced by setting $\mathscr{P}_{K+1} = \mathscr{P}_{K-1}$ and $\mathscr{P}_{K+n_x} = \mathscr{P}_{K-n_x}$. Since positions $K - 1$ and $K - n_x$ correspond to grain voxels in this case, equation (2.3) is rewritten as

$$\frac{1}{h_z^2}\mathscr{P}_{K+n_x n_y} + \frac{2}{h_y^2}\mathscr{P}_{K+n_x} + \frac{2}{h_x^2}\mathscr{P}_{K+1} - \left(\frac{2}{h_x^2} + \frac{2}{h_y^2} + \frac{2}{h_z^2}\right)\mathscr{P}_K + \frac{1}{h_z^2}\mathscr{P}_{K-n_x n_y} = 0. \quad (2.9)$$

At grain voxels the pressure is set to zero as a dummy value, which will not influence the velocity calculation on the next step.

The n_{xyz} equations can now be described by the matrix equation

$$
\begin{bmatrix}
\alpha & \frac{2}{h_x^2} & 0...0 & \frac{2}{h_y^2} & 0...0 & \frac{2}{h_z^2} & 0... & & & & & & & & \\
\frac{1}{h_x^2} & \alpha & \frac{1}{h_x^2} & 0...0 & \frac{2}{h_y^2} & 0...0 & \frac{2}{h_z^2} & 0... & & & & & & & \\
 & & \ddots & & & & & & & & & & & & \\
...\frac{1}{h_y^2} & 0...0 & \frac{1}{h_x^2} & \alpha & \frac{1}{h_x^2} & 0...0 & \frac{1}{h_y^2} & 0...0 & \frac{1}{h_z^2} & 0... & & & & & \\
...0 & \frac{1}{h_y^2} & 0...0 & \frac{1}{h_x^2} & \alpha & \frac{1}{h_x^2} & 0...0 & \frac{1}{h_y^2} & 0...0 & \frac{1}{h_z^2} & 0... & & & & \\
...\frac{1}{h_z^2} & 0...0 & \frac{1}{h_y^2} & 0...0 & \frac{1}{h_x^2} & \alpha & \frac{1}{h_x^2} & 0...0 & \frac{1}{h_y^2} & 0...0 & \frac{1}{h_z^2} & 0... & & & \\
...0 & \frac{1}{h_z^2} & 0...0 & \frac{1}{h_y^2} & 0...0 & \frac{1}{h_x^2} & \alpha & \frac{1}{h_x^2} & 0...0 & \frac{1}{h_y^2} & 0...0 & \frac{1}{h_z^2} & 0... & & \\
 & ...0 & \frac{1}{h_z^2} & 0...0 & \frac{1}{h_y^2} & 0...0 & \frac{1}{h_x^2} & \alpha & \frac{1}{h_x^2} & 0...0 & \frac{1}{h_y^2} & 0...0 & \frac{1}{h_z^2}... & & \\
 & & ...0 & \frac{1}{h_z^2} & 0...0 & \frac{1}{h_y^2} & 0...0 & \frac{1}{h_x^2} & \alpha & \frac{1}{h_x^2} & 0...0 & \frac{1}{h_y^2} & 0... & & \\
 & & & ...0 & \frac{1}{h_z^2} & 0...0 & \frac{1}{h_y^2} & 0...0 & \frac{1}{h_x^2} & \alpha & \frac{1}{h_x^2} & 0...0 & \frac{1}{h_y^2}... & & \\
 & & & & & & & & & \ddots & & & & & \\
 & & & & & ...0 & \frac{2}{h_z^2} & 0...0 & \frac{2}{h_y^2} & 0...0 & \frac{1}{h_x^2} & \alpha & \frac{1}{h_x^2} & & \\
 & & & & & & ...0 & \frac{2}{h_z^2} & 0...0 & \frac{2}{h_y^2} & 0...0 & \frac{2}{h_x^2} & \alpha & &
\end{bmatrix}
\begin{bmatrix}
\mathscr{P}_1 \\ \mathscr{P}_2 \\ \vdots \\ \mathscr{P}_{K+n_{xy}} \\ \mathscr{P}_{K+n_x} \\ \mathscr{P}_{K+1} \\ \mathscr{P}_K \\ \mathscr{P}_{K-1} \\ \mathscr{P}_{K-n_x} \\ \mathscr{P}_{K-n_{xy}} \\ \vdots \\ \mathscr{P}_{N-1} \\ \mathscr{P}_N
\end{bmatrix}
=
\begin{bmatrix}
-\frac{\mathscr{P}_{in}}{h_z^2} \\ -\frac{\mathscr{P}_{in}}{h_z^2} \\ \vdots \\ 0 \\ 0 \\ 0 \\ 0 \\ 0 \\ 0 \\ 0 \\ \vdots \\ -\frac{\mathscr{P}_{out}}{h_z^2} \\ -\frac{\mathscr{P}_{out}}{h_z^2}
\end{bmatrix}
\tag{2.10}
$$

where $\alpha = -\left(\frac{2}{h_x^2} + \frac{2}{h_y^2} + \frac{2}{h_z^2}\right)$. This system is in the traditional form

$$\boxed{\mathbf{Ax} = \mathbf{b}}, \tag{2.11}$$

where $\mathbf{A}$ is finite difference Laplacian operator, $\mathbf{x}$ is the vector of unknowns and $\mathbf{b}$ is the vector of results at the righthand side of equation (2.10). We will use bold letters for finite differences solution vectors.

2.1.2 Discretization of velocity field equation

Once the pressure field is calculated, it is used as a forcing function to solve Poisson's equation for velocity (equation (1.7)). In principle, equation (1.7) can be solved separately in each direction, leading to a set of Poisson equations for the scalar velocity

components v_x, v_y and v_z,

$$\nabla^2 v_x = \frac{1}{\mu}\frac{\partial \mathscr{P}}{\partial x}, \tag{2.12}$$

$$\nabla^2 v_y = \frac{1}{\mu}\frac{\partial \mathscr{P}}{\partial y}, \tag{2.13}$$

$$\nabla^2 v_z = \frac{1}{\mu}\frac{\partial \mathscr{P}}{\partial z}, \tag{2.14}$$

whose discretization would be analogous to the pressure case. Pressure gradients are calculated by central first finite difference,

$$\frac{\partial \mathscr{P}}{\partial x} \approx \frac{\mathscr{P}_{i+1,j,k} - \mathscr{P}_{i-1,j,k}}{2h_x}, \tag{2.15}$$

$$\frac{\partial \mathscr{P}}{\partial y} \approx \frac{\mathscr{P}_{i,j+1,k} - \mathscr{P}_{i,j-1,k}}{2h_y}, \tag{2.16}$$

$$\frac{\partial \mathscr{P}}{\partial z} \approx \frac{\mathscr{P}_{i,j,k+1} - \mathscr{P}_{i,j,k-1}}{2h_z}. \tag{2.17}$$

No slip and no penetration boundary conditions are imposed by setting zero velocity at the grain voxels, and the directional derivatives for velocity are set to zero at the open boundaries. However, even if the pressure field is estimated using the zero divergence condition for velocity, its use as a forcing function does not guarantee a zero divergence velocity field, as also pointed by Nördstrom *et al.* [42]. Moreover, although the fully developed flow profile can be achieved by this set of boundary conditions, they also lead to a system with non unique solution.

This project uses a different approach to couple Stokes equation and the zero divergence constraint. Let $\mathbf{A}$ be the Laplacian operator matrix as was done for the pressure field, $\mathbf{b_x}$, $\mathbf{b_y}$, and $\mathbf{b_z}$ be the respectively the pressure gradient in x, y, and z directions, divided by viscosity and indexed as in equation (2.2), and $\mathbf{D}$ be the divergence operator matrix formed

from the set of equations

$$\vec{\nabla} \cdot \vec{v}(x,y,z) \approx \frac{v_x^{i+1,j,k} - v_x^{i-1,j,k}}{2h_x} + \frac{v_y^{i,j+1,k} - v_y^{i,j-1,k}}{2h_y} + \frac{v_z^{i,j,k+1} - v_z^{i,j,k-1}}{2h_y}$$

$$= \frac{v_x^{K+1} - v_x^{K-1}}{2h_x} + \frac{v_y^{K+n_x} - v_y^{K-n_x}}{2h_y} + \frac{v_z^{K+n_x n_y} - v_z^{K-n_x n_y}}{2h_y}. \quad (2.18)$$

The problem can now be reformulated as to solve the $3n_{xyz} \times 3n_{xyz}$ system formed by the block matrices

$$\begin{bmatrix} \mathbf{A}_x & \mathbf{0} & \mathbf{0} \\ \mathbf{0} & \mathbf{A}_y & \mathbf{0} \\ \mathbf{0} & \mathbf{0} & \mathbf{A}_z \end{bmatrix} \begin{bmatrix} \mathbf{v_x} \\ \mathbf{v_y} \\ \mathbf{v_z} \end{bmatrix} = \begin{bmatrix} \mathbf{b_x} \\ \mathbf{b_y} \\ \mathbf{b_z} \end{bmatrix} \quad (2.19)$$

subject to

$$\mathbf{D} \begin{bmatrix} \mathbf{v_x} \\ \mathbf{v_y} \\ \mathbf{v_z} \end{bmatrix} = \mathbf{0}. \quad (2.20)$$

For simplicity, let

$$\mathbf{L} \equiv \begin{bmatrix} \mathbf{A}_x & \mathbf{0} & \mathbf{0} \\ \mathbf{0} & \mathbf{A}_y & \mathbf{0} \\ \mathbf{0} & \mathbf{0} & \mathbf{A}_z \end{bmatrix}, \quad \mathbf{v} \equiv \begin{bmatrix} \mathbf{v_x} \\ \mathbf{v_y} \\ \mathbf{v_z} \end{bmatrix}, \quad \mathbf{b} \equiv \begin{bmatrix} \mathbf{b_x} \\ \mathbf{b_y} \\ \mathbf{b_z} \end{bmatrix}. \quad (2.21)$$

We use an approach analogous to the Tikhonov regularization [64] to change the problem to finding

$$\min \left\{ \|\mathbf{Lv} - \mathbf{b}\|_2^2 + \lambda^2 \|\mathbf{Dv}\|_2^2 \right\} \quad (2.22)$$

for some positive parameter λ. A little bit of matrix algebra allows to transform the above

expression:

$$
\begin{aligned}
\|\mathbf{Lv}-\mathbf{b}\|_2^2+\lambda^2\|\mathbf{Dv}\|_2^2 &= (\mathbf{Lv}-\mathbf{b})^T(\mathbf{Lv}-\mathbf{b})+\lambda^2(\mathbf{Dv})^T\mathbf{Dv} \\
&= (\mathbf{v}^T\mathbf{L}^T-\mathbf{b}^T)(\mathbf{Lv}-\mathbf{b})+\lambda^2\mathbf{v}^T\mathbf{D}^T\mathbf{Dv} \\
&= \mathbf{v}^T\mathbf{L}^T\mathbf{Lv}-\mathbf{v}^T\mathbf{L}^T\mathbf{b}-\mathbf{b}^T\mathbf{Lv}+\mathbf{b}^T\mathbf{b}+\lambda^2\mathbf{v}^T\mathbf{D}^T\mathbf{Dv} \\
&= \mathbf{v}^T(\mathbf{L}^T\mathbf{L}+\lambda^2\mathbf{D}^T\mathbf{D})\mathbf{v}-\mathbf{v}^T\mathbf{L}^T\mathbf{b}-\mathbf{b}^T\mathbf{Lv}+\mathbf{b}^T\mathbf{b} \\
&= \mathbf{v}^T\begin{bmatrix}\mathbf{L}^T & \lambda\mathbf{D}\end{bmatrix}\begin{bmatrix}\mathbf{L}\\ \lambda\mathbf{D}\end{bmatrix}\mathbf{v}-\mathbf{v}^T\begin{bmatrix}\mathbf{L}^T & \lambda\mathbf{D}\end{bmatrix}\begin{bmatrix}\mathbf{b}\\ \mathbf{0}\end{bmatrix} \\
&\qquad -\begin{bmatrix}\mathbf{b}^T & \mathbf{0}\end{bmatrix}\begin{bmatrix}\mathbf{L}\\ \lambda\mathbf{D}\end{bmatrix}\mathbf{v}+\begin{bmatrix}\mathbf{b}^T & \mathbf{0}\end{bmatrix}\begin{bmatrix}\mathbf{b}\\ \mathbf{0}\end{bmatrix} \\
&= \left(\mathbf{v}^T\begin{bmatrix}\mathbf{L}^T & \lambda\mathbf{D}\end{bmatrix}-\begin{bmatrix}\mathbf{b}^T & \mathbf{0}\end{bmatrix}\right)\left(\begin{bmatrix}\mathbf{L}\\ \lambda\mathbf{D}\end{bmatrix}\mathbf{v}-\begin{bmatrix}\mathbf{b}\\ \mathbf{0}\end{bmatrix}\right) \\
&= \left(\begin{bmatrix}\mathbf{L}\\ \lambda\mathbf{D}\end{bmatrix}\mathbf{v}-\begin{bmatrix}\mathbf{b}\\ \mathbf{0}\end{bmatrix}\right)^T\left(\begin{bmatrix}\mathbf{L}\\ \lambda\mathbf{D}\end{bmatrix}\mathbf{v}-\begin{bmatrix}\mathbf{b}\\ \mathbf{0}\end{bmatrix}\right) \\
&= \left\|\begin{bmatrix}\mathbf{L}\\ \lambda\mathbf{D}\end{bmatrix}\mathbf{v}-\begin{bmatrix}\mathbf{b}\\ \mathbf{0}\end{bmatrix}\right\|_2^2. \qquad (2.23)
\end{aligned}
$$

Thus, the constrained problem is equivalent to a least squares problem,

$$
\min\left\{\|\mathbf{Lv}-\mathbf{b}\|_2^2+\lambda^2\|\mathbf{Dv}\|_2^2\right\} \Longleftrightarrow \min\left\{\left\|\begin{bmatrix}\mathbf{L}\\ \lambda\mathbf{D}\end{bmatrix}\mathbf{v}-\begin{bmatrix}\mathbf{b}\\ \mathbf{0}\end{bmatrix}\right\|_2^2\right\}, \qquad (2.24)
$$

whose solution immediately follows from the normal equations:

$$
[\mathbf{L^T}\ \lambda\mathbf{D}]\begin{bmatrix}\mathbf{L}\\ \lambda\mathbf{D}\end{bmatrix}\mathbf{v}=[\mathbf{L^T}\ \lambda\mathbf{D}]\begin{bmatrix}\mathbf{b}\\ \mathbf{0}\end{bmatrix}, \qquad (2.25)
$$

$$\boxed{(\mathbf{L}^T\mathbf{L} + \lambda^2\mathbf{D}^T\mathbf{D})\mathbf{v} = \mathbf{L}^T\mathbf{b}}. \tag{2.26}$$

2.1.3 Discretization of electric potential field equation

For the electric potential estimation, a normalized value of conductivity is assigned to each voxel, according to the segmentation process. If the segmentation objective is to divide the sample in only two phases (pore/grain) with electrical insulating grains, then pore phase conductivity is set to 1 and grain phase conductivity is set to zero[1]. Equation (1.35) simplifies to a Laplace equation, and the solution for pressure field and electric potential field will be numerically identical, since the two problems share the same boundary conditions. However, conducting grain phases like clay or metallic minerals or voxels containing a mixture of grain and pore may require different values of electrical conductivity, requiring the solution of equation (1.35) in its original form.

A stable system of linear equations is achieved with the following procedure: first, we rewrite this equation as

$$\frac{\partial}{\partial x}\left[\sigma\left(\frac{\partial \varphi}{\partial x}\right)\right] + \frac{\partial}{\partial y}\left[\sigma\left(\frac{\partial \varphi}{\partial y}\right)\right] + \frac{\partial}{\partial z}\left[\sigma\left(\frac{\partial \varphi}{\partial z}\right)\right] = 0 \tag{2.27}$$

and then use central finite differences with half of each voxel length,

$$\frac{\partial}{\partial x}\left(\sigma_{i,j,k}\frac{\varphi_{i+\frac{1}{2},j,k} - \varphi_{i-\frac{1}{2},j,k}}{h_x}\right) + \frac{\partial}{\partial y}\left(\sigma_{i,j,k}\frac{\varphi_{i,j+\frac{1}{2},k} - \varphi_{i,j-\frac{1}{2},k}}{h_y}\right) + \frac{\partial}{\partial z}\left(\sigma_{i,j,k}\frac{\varphi_{i,j,k+\frac{1}{2}} - \varphi_{i,j,k-\frac{1}{2}}}{h_z}\right) = 0, \tag{2.28}$$

[1]Values greater than 1 for pore voxel conductivity would scale the effective conductivity, whose final value would need to be normalized.

$$\frac{1}{h_x}\left[\left(\sigma_{i+\frac{1}{2},j,k}\frac{\varphi_{i+1,j,k}-\varphi_{i,j,k}}{h_x}\right)-\left(\sigma_{i-\frac{1}{2},j,k}\frac{\varphi_{i,j,k}-\varphi_{i-1,j,k}}{h_x}\right)\right]$$
$$+\frac{1}{h_y}\left[\left(\sigma_{i,j+\frac{1}{2},k}\frac{\varphi_{i,j+1,k}-\varphi_{i,j,k}}{h_y}\right)-\left(\sigma_{i,j-\frac{1}{2},k}\frac{\varphi_{i,j,k}-\varphi_{i,j-1,k}}{h_y}\right)\right]$$
$$+\frac{1}{h_z}\left[\left(\sigma_{i,j,k+\frac{1}{2}}\frac{\varphi_{i,j,k+1}-\varphi_{i,j,k}}{h_z}\right)-\left(\sigma_{i,j,k-\frac{1}{2}}\frac{\varphi_{i,j,k}-\varphi_{i,j,k-1}}{h_z}\right)\right]=0. \quad (2.29)$$

Now we use the upwind interpolation, where the conductivity at half step in the discrete network of electrical conductors is assumed do be equal to the one we get rounding down the indices. This assumption results in the equation

$$\frac{1}{h_x}\left[\left(\sigma_{i,j,k}\frac{\varphi_{i+1,j,k}-\varphi_{i,j,k}}{h_x}\right)-\left(\sigma_{i-1,j,k}\frac{\varphi_{i,j,k}-\varphi_{i-1,j,k}}{h_x}\right)\right]$$
$$+\frac{1}{h_y}\left[\left(\sigma_{i,j,k}\frac{\varphi_{i,j+1,k}-\varphi_{i,j,k}}{h_y}\right)-\left(\sigma_{i,j-1,k}\frac{\varphi_{i,j,k}-\varphi_{i,j-1,k}}{h_y}\right)\right]$$
$$+\frac{1}{h_z}\left[\left(\sigma_{i,j,k}\frac{\varphi_{i,j,k+1}-\varphi_{i,j,k}}{h_z}\right)-\left(\sigma_{i,j,k-1}\frac{\varphi_{i,j,k}-\varphi_{i,j,k-1}}{h_z}\right)\right]=0. \quad (2.30)$$

Using the linear indexing provided in equation (2.2), we get the system of equations

$$\left(\frac{\sigma_K}{h_z^2}\right)\varphi_{K+n_xn_y}+\left(\frac{\sigma_K}{h_y^2}\right)\varphi_{K+n_x}+\left(\frac{\sigma_K}{h_x^2}\right)\varphi_{K+1}$$
$$-\left(\frac{\sigma_K+\sigma_{K-1}}{h_x^2}+\frac{\sigma_K+\sigma_{K-n_x}}{h_y^2}+\frac{\sigma_K+\sigma_{K-n_xn_y}}{h_z^2}\right)\varphi_K$$
$$+\left(\frac{\sigma_{K-1}}{h_x^2}\right)\varphi_{K-1}+\left(\frac{\sigma_{K-n_x}}{h_y^2}\right)\varphi_{K-n_x}+\left(\frac{\sigma_{K-n_xn_y}}{h_z^2}\right)\varphi_{K-n_xn_y}=0. \quad (2.31)$$

Boundary conditions and computational implementation are similar to the calculation of the pressure field.

Table 2.1: Approximate file sizes for the implemented data formats. Total size consider two segmented files (segmentation and connectivity) and five scalar fields (pressure, velocity components and electric potential).

Sample size ($n_x \times n_y \times n_z$)	Number of voxels	Segmentation data file size	Scalar field data file size	Total size
250×250×250	15,625,000	15 MB	60 MB	330 MB
500×500×500	125,000,000	120 MB	477 MB	2.56 GB
1000×1000×1000	1,000,000,000	950 MB	3.7 GB	20.3 GB

2.2 Implementation details and workflow outline

All the routines were implemented using C programming language with shared-memory parallel computing OpenMP API[2]. Calculations were performed using Lonestar Linux high performance computer at Texas Advanced Computer Center[3]. Each simulation used one computer node with two Xeon 5680 series 3.33GHz hex-core processors (12 cores total) sharing 24GB of memory[4].

2.2.1 Data format

Data files are stored in raw data format, each file containing an array of values for each voxel following the indexation in equation (2.2). Segmented data are stored in 8 bit integer format, allowing up to $2^8 = 256$ phases. Due to the potentially large amount of memory for big samples, scalar fields (pressure, electric potential and each component of the velocity field) are stored as single precision (4 bytes) floating point format. Sample size and phase properties are provided as separate files in ASCII format, to facilitate testing different scenarios for the same sample. Table 2.1 exemplifies file sizes for the chosen formats.

[2]http://openmp.org
[3]https://www.tacc.utexas.edu
[4]https://www.tacc.utexas.edu/resources/hpc/lonestar

2.2.2 Porosity calculation

The porosity calculation simply average the porosity value for each voxel throughout the sample. However, on big samples, the increment on the cumulative number of pore voxels can rapidly fall below the machine precision, due to the large number of voxels to be counted (see Table 2.1). To get accurate values on big samples, a simple solution is applied: first, the porosity is averaged along one line of voxels and the value is stored in a auxiliary variable. Then, the same calculation is repeated to all the lines in the same slice, accumulating each result on the auxiliary variable. The slice porosity is then obtained by dividing the cumulative value by the number of lines in the slice. The process is repeated to all the slices, accumulating the value in a second auxiliary variable. The final value of porosity will then be accurately described by the average of the slices' porosities.

2.2.3 Connectivity of the conducting phase

To prevent a result of non zero flow in a disconnected space, the connectivity of fluid/electrical conducting phase is evaluated before the routines to calculate the scalar fields are used. In this project, two voxels are considered connected if they have a face in common, what is also known as 6-connectivity. The routine is a grass fire-like algorithm. It starts assigning a label equal to 1 for each pore/conducting voxel at the inlet xy slice and zero elsewhere in the domain. An iterative process reassigns the voxel label to 1 if any of its neighbors is also labeled 1 and repeats until there is no change in the labels. The voxels labeled as 1 will have a connected path to the inlet face. Within these voxels, similar calculation is performed to find the ones with a connected path to the outlet face. At the end, only voxels with a percolating path though the sample will remain labeled as 1. The result is stored as a segmentation type file. Only voxels connected to both ends are used to calculate the scalar fields.

2.2.4 Pressure/electric potential

The described discretizations led to a set of linear equations $\mathbf{Ax} = \mathbf{b}$ for each studied phenomenon. For pressure and electrical potential fields, the coefficient matrix $\mathbf{A}$ is heptadiagonal, although non symmetrical due to the chosen boundary conditions and the irregularity of the porous media. The size of the full matrix is equal to the number of voxels squared, which is impossible to store in a computer memory for reasonable sample sizes. One alternative could be the band storage (storage of the diagonals in the band) but direct solution methods such as LU decomposition create non-zero values inside the matrix band, wasting the available computer memory and limiting the applicability to small samples.

The sparsity of the coefficient matrix makes the system suitable for iterative methods [65]. A fast and memory efficient linear solver capable of handling huge matrices can be built by using the biconjugate gradient stabilized method, whose details can be found in the work of Van der Vorst [66].

System preconditioning is used to make convergence faster. A preconditioner $\mathbf{K}$ of a matrix $\mathbf{A}$ is a matrix built such that the operation $\mathbf{K}^{-1}\mathbf{A}$ has a better condition number. Thus, the solution of the system of equations given by $\mathbf{K}^{-1}\mathbf{Ax} = \mathbf{K}^{-1}\mathbf{b}$ will converge faster and will have the same solution as the original system $\mathbf{Ax} = \mathbf{b}$ (see [65] for preconditioning techniques). Since $\mathbf{A}$ is diagonal dominant, the Jacobi preconditioner, defined as a diagonal matrix with the main diagonal of $\mathbf{A}$, gives a good compromise between simplicity and convergence speed.

The preconditioned biconjugate gradient stabilized method, is stated below:

1. From an initial guess $\mathbf{x}_0$, let $\mathbf{r}_0 = \mathbf{b} - \mathbf{Ax}_0$;
2. Choose $\hat{\mathbf{r}}_0$ as an arbitrary vector, such that $(\hat{\mathbf{r}}_0, \mathbf{r}_0) \neq 0$, for example $\hat{\mathbf{r}}_0 = \mathbf{r}_0$;
3. $\rho_0 = \alpha = \omega_0 = 1$;
4. $\mathbf{v}_0 = \mathbf{p}_0 = \mathbf{0}$;
5. for $i = 1, 2, 3 \ldots$

(a) $\rho_i = (\hat{\mathbf{r}}_0, \mathbf{r}_{i-1})$

(b) $\beta = (\rho_i/\rho_{i-1})(\alpha/\omega_{i-1})$

(c) $\mathbf{p}_i = \mathbf{r}_{i-1} + \beta(\mathbf{p}_{i-1} - \omega_{i-1}\mathbf{v}_{i-1})$;

(d) $\mathbf{y} = \mathbf{K}^{-1}\mathbf{p}_i$;

(e) $\mathbf{v}_i = \mathbf{A}\mathbf{y}$;

(f) $\alpha = \rho_i/(\hat{\mathbf{r}}_0, \mathbf{v}_i)$;

(g) $\mathbf{s} = \mathbf{r}_{i-1} - \alpha\mathbf{v}_i$;

(h) $\mathbf{z} = \mathbf{K}^{-1}\mathbf{s}$;

(i) $\mathbf{t} = \mathbf{A}\mathbf{z}$;

(j) $\omega_i = (\mathbf{K}^{-1}\mathbf{t}, \mathbf{K}^{-1}\mathbf{s})/(\mathbf{K}^{-1}\mathbf{t}, \mathbf{K}^{-1}\mathbf{t})$;

(k) $\mathbf{x}_i = \mathbf{x}_{i-1} + \alpha\mathbf{y} + \omega_i\mathbf{z}$;

(l) $\mathbf{r}_i = \mathbf{s} - \omega_i\mathbf{t}$;

(m) if $\|\mathbf{r}_i\|$ is less than a predefined tolerance, then quit;

end

The initial guess is taken as a constant gradient in z direction, and the operation $(\cdot, \cdot)$ denotes scalar product between two vectors. Note that this method does not require the matrix $\mathbf{A}$, but its multiplication by a vector. Since the matrix $\mathbf{A}$ is defined by equations (2.3), (2.31) and their analogues at domain boundaries, effective $\mathbf{Ax}$ calculations can be done by explicitly using those equations, allowing to solve the problem without actually storing any part of the matrix. The major part of the required memory is used to allocate the nine auxiliary vectors. Table 2.2 compares the approximate memory required by this method and the traditional ones.

2.2.5 Velocity field

The velocity field is calculated in two steps. First, from zero velocity as initial guess, the three components are independently estimated from Stokes equation. The same Poisson solver used to calculate pressure and electric potential is also used in this stage, with the respective components of pressure gradients as the forcing function.

Table 2.2: Approximate computer memory required to solve for a scalar field, considering single precision floating point data type (4 bytes per number). Matrix size equals the number of voxels squared.

Sample size ($n_x \times n_y \times n_z$)	Number of voxels	Matrix inv. (full size)	LU dec. with banded storage	Biconj. grad. stabilized
250×250×250	15,625,000	888 TB	14 TB	536 MB
500×500×500	125,000,000	55 PB	454 TB	4.2 GB
1000×1000×1000	1,000,000,000	3550 PB	14 PB	33 GB

Next, this intermediate solution for velocity is used as an initial guess for equation (2.26) in order to calculate the incompressible velocity field. The coefficient matrix $\mathbf{L}^T\mathbf{L} + \lambda^2\mathbf{D}^T\mathbf{D}$ is now symmetric, allowing to use the conjugate gradient method [65] as the linear solver, which requires less amount of computational memory compared to the biconjugate gradient stabilized method. Preconditioned conjugate gradient method is listed below.

1. From an initial guess $\mathbf{x}_0$, let $\mathbf{r}_0 = \mathbf{b} - \mathbf{A}\mathbf{x}_0$;
2. $\mathbf{z}_0 = \mathbf{K}^{-1}\mathbf{x}_0$
3. $\mathbf{p}_0 = \mathbf{z}_0$;
4. for $i = 0, 1, 2 \ldots$
   (a) $\alpha_i = (\mathbf{r}_i, \mathbf{z}_i)/(\mathbf{p}_i, \mathbf{A}\mathbf{p}_i)$
   (b) $\mathbf{x}_{i+1} = \mathbf{x}_i + \alpha_i\mathbf{p}_i$
   (c) $\mathbf{r}_{i+1} = \mathbf{r}_i - \alpha_i\mathbf{A}\mathbf{p}_i$
   (d) if $\mathbf{r}_{i+1}$ is small enough then quit;
   (e) $\mathbf{z}_{i+1} = \mathbf{K}^{-1}\mathbf{r}_{i+1}$;
   (f) $\beta_i = (\mathbf{z}_{i+1}, \mathbf{r}_{i+1})/(\mathbf{z}_i, \mathbf{r}_i)$;
   (g) $\mathbf{p}_{i+1} = \mathbf{z}_{i+1} + \beta_i\mathbf{p}_i$;

   end

Although this method only requires four auxiliary vectors, the vector sizes are three times bigger than the ones for scalar fields. Approximate memory requirements are listed in Table 2.3. Some numerical problems also arise. First, the coefficient matrix $\mathbf{A} = \mathbf{L}^T\mathbf{L} +$

Table 2.3: Approximate computer memory required to solve for a vector field, considering single precision floating point data type (4 bytes per number). Matrix size equals the number of voxels squared.

Sample size ($n_x \times n_y \times n_z$)	Number of voxels	Conjugate graditent
250×250×250	15,625,000	1.04 GB
500×500×500	125,000,000	8.38 GB
1000×1000×1000	1,000,000,000	67 GB

$\lambda^2\mathbf{D}^T\mathbf{D}$ is now a full matrix, but sparsity of $\mathbf{L}$ and $\mathbf{D}$ can still be used to compute the product $\mathbf{Ax}$ in a few steps. Besides the increased number of operations, the high condition number resulting from the product by the transpose matrix lowers the rate of convergence considerably and raises the sensitivity to roundoff errors. The Jacobi preconditioner and parallel computing still are used to speed-up the convergence, but a better preconditioner needs to be implemented in future improvements of the computational code.

2.2.6 Permeability estimation

In order to estimate bulk hydraulic permeability, the volumetric flux in z direction is calculated for each xy slice as

$$\Phi_z(z) = \oint v_z dA, \tag{2.32}$$

where A is the area of the k^{th} xy slice. The flow rate Q through the porous medium is then assumed to be the average value of Φ_z across the whole sample. Then, from Darcy's equation, final value for permeability is

$$k = \frac{Q\mu L}{A(p_{in} - p_{out})}, \tag{2.33}$$

where L is the sample length in z direction and A is the area of one xy slice. The ratio of the standard deviation to the mean value of $\Phi_z(z)$ defines the relative error for the estimated permeability.

2.2.7 Bulk electrical conductivity

From electric potential, the electric current density is obtained by numerically evaluating

$$\vec{J} = \sigma \vec{\nabla} \varphi. \tag{2.34}$$

Then, the electric current I through each xy slice is calculated using the definition

$$I(z) = \oint \vec{J} \cdot \hat{n} dA, \tag{2.35}$$

over each xy slice with $\hat{n}$ pointing to positive z direction. Finally, Ohm's law gives the normalized electrical conductivity,

$$\hat{\sigma} = \frac{L\bar{I}}{A\Delta V}, \tag{2.36}$$

where $\bar{I}$ is the average value of the electric current, L is the sample length in z direction, A is the area of an xy slice and ΔV is the potential difference between the first and the last xy slice. The ratio of the standard deviation to the mean value of $I(z)$ defines the relative error in $\hat{\sigma}$. Formation factor is the reciprocal of the normalized conductivity.

2.3 Testing samples

2.3.1 Benchmarks

The first group of datasets used to validate the algorithms consists of three established benchmarks:

- a 500^3 disordered close pack of non overlapping equally-sized spheres, digitally generated from Finney's experimental data [3]. The voxel size was chosen to be 3 μm, in order to match the two other datasets. Sphere diameter is equal to 50 voxels.
- a 500^3 Fontainebleau sandstone with voxel size equal to 3 μm;
- a 500^3 sucrosic dolomite also with voxel size equal to 3 μm.

Details about the image segmentation for the sandstone and the dolomite samples can be found in [67]. Figure 2.1 shows these three data sets.

2.3.2 Numerical cementation and dissolution of digitized rock samples

Numerical procedures to simulate cementation have been used to study the mechanisms of porosity reduction in sandstone [6]. Mousavi and Bryant [68] model tight gas sands by using uniform cement overgrowth on a spherical packing, simulating plastic deformation by allowing superposition of part of the grains. In a more recent work, Prodanović *et al.* [69] use a level set based method to simulate cement overgrowth on a segmented X-ray microtomography image.

We simulate cementation on the Finney pack sample by operation of dilation on the segmented image. In a dilation process, each voxel value is replaced by the maximum value in a $3 \times 3 \times 3$ neighborhood centered on that voxel. The inverse operation, called erosion, can simulate grain dissolution and generate fluid supported material. An erosion procedure replaces the voxel value with the minimum in the same neighborhood.

A total of 20 samples were generated by repeatedly applying these processes on the original pack using the open source image processing package Fiji[5].

[5]http://fiji.sc/Fiji

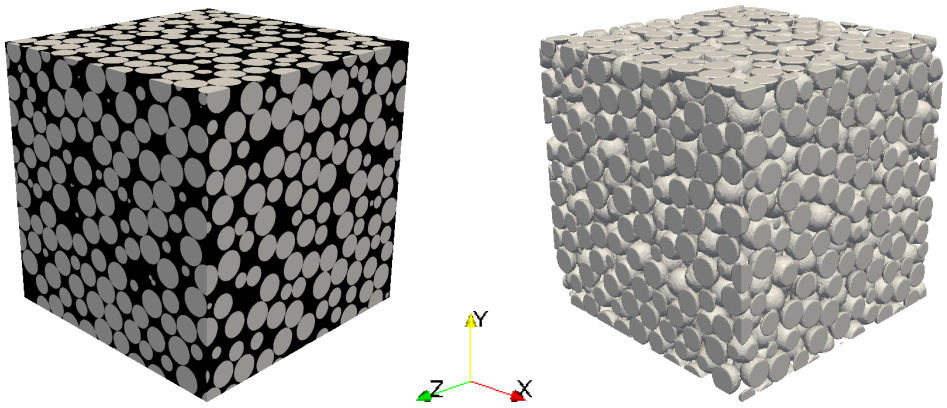

(a) Finney pack

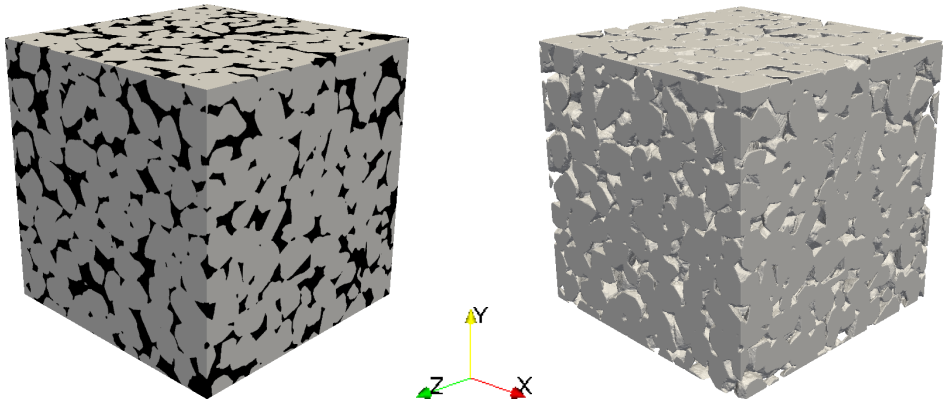

(b) Fontainebleau sandstone

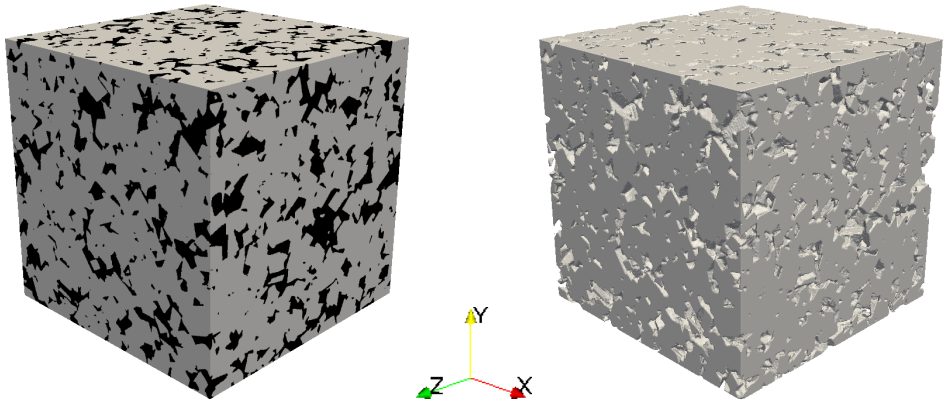

(c) Dolomite

Figure 2.1: Benchmark samples used to test the algorithms. All the samples have dimensions equal to $500 \times 500 \times 500$ voxels and voxel size equal to 3 μm. Left: segmented images with black pores and gray grains; right: 3D rendering of pore-grain phase. The images were generated with the open source visualization application Paraview (http://www.paraview.org).

2.3.3 Multiphase fluid distribution for Fontainebleau sandstone

We obtained a two-phase fluid distribution in a 250^3 subset of the Fontainebleau sandstone, from a drainage simulation as described in [61], using the level set based progressive *quasi*-static algorithm (LSMPQS) [59]. The simulation consists of a capillary dominated two-phase fluid flow, with an initial planar non wetting phase front trying to invade the pore space 100% saturated with the wetting phase. The rock is considered to be perfectly wet by the wetting fluid (zero contact angle).

The simulation goal is to find, for each increasing value of the capillary pressure p_c, the equilibrium curved interface between the wetting and the non wetting phases that obeys Young-Laplace equation

$$p_c = \gamma C. \tag{2.37}$$

Here, γ is the interfacial tension and C is the curvature of the interface. On the method formulation, a level set function $\phi(x, y, z, \tau)$, initially at $\phi(x, y, z, 0)$, evolves in time τ following the partial differential equation

$$\frac{\partial \phi}{\partial \tau} + F|\vec{\nabla}\phi| = 0, \tag{2.38}$$

where $F(x, y, z, \tau)$ is the normal component of the interface velocity. To apply this technique to the drainage simulation, the *quasi*-static movement is governed by

$$F(x, y, z, \tau) = p_c - \gamma C(x, y, z, \tau), \tag{2.39}$$

and the equilibrium interface is taken as the zero level set of the solution of equation (2.38), the set of points such that $\phi(x, y, z, \tau) = 0$.

The simulation generated a set of 10 fluid configurations, some of them illustrated in Figure 2.2, that will be used to investigate relative permeability and resistivity index for

the Fontainebleau sandstone. The corresponding drainage curve is shown in Figure 2.3. LSMPQS is implemented using C/FORTRAN computer languages and can be downloaded at the author's web page[6].

2.3.4 Outcrop samples with lab data

The last group of samples consists of original μ-CT images for plugs from outcrops of a Bentheimer sandstone a Buff Berea sandstone and an Idaho Brown sandstone. The three data sets consist of $1000 \times 1000 \times 1500$ voxel images. Voxel size for Bentheimer and Idaho sandstones is equal to 5 μm, while voxel size for Buff Berea sandstone is 2 μm. Datasets and respective routine core analysis results are courtesy of Petrobras Research Center, Brazil.

Figure 2.4 shows laboratory data for porosity and permeability measured in sister samples from the same outcrops. Figures 2.5, 2.6, and 2.7 show slices of the original 3D μ-CT images. In order to fit the 24 GB of shared memory available on the computer nodes used (see again Table 2.2 on page 33), each of these three samples were divided in twelve 500^3 subsamples and the corresponding electric and velocity fields where calculated. These properties were also calculated in copies of the full samples upscaled to twice the voxel size ($500 \times 500 \times 750$ voxels) to investigate variation with resolution.

2.3.5 Segmentation of imaged samples

We used the image processing package Fiji to perform the image segmentation in three steps. First, a $2 \times 2 \times 2$ median filter was applied to slightly reduce the noise level, while trying to preserve pore-grain edges. For more information on image filtering and noise reduction see [28].

Second, a procedure called statistical region merging [70] was applied. This procedure starts defining each voxel as an independent region, and successively performs sta-

[6] `http://users.ices.utexas.edu/ masha/lsmpqs/index.html`.

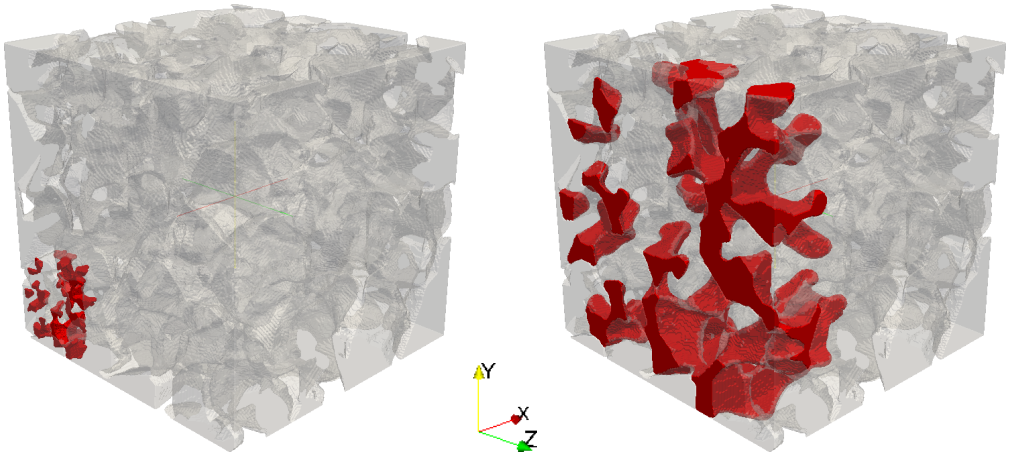

(a) $S_w = 85\%$ (b) $S_w = 79\%$

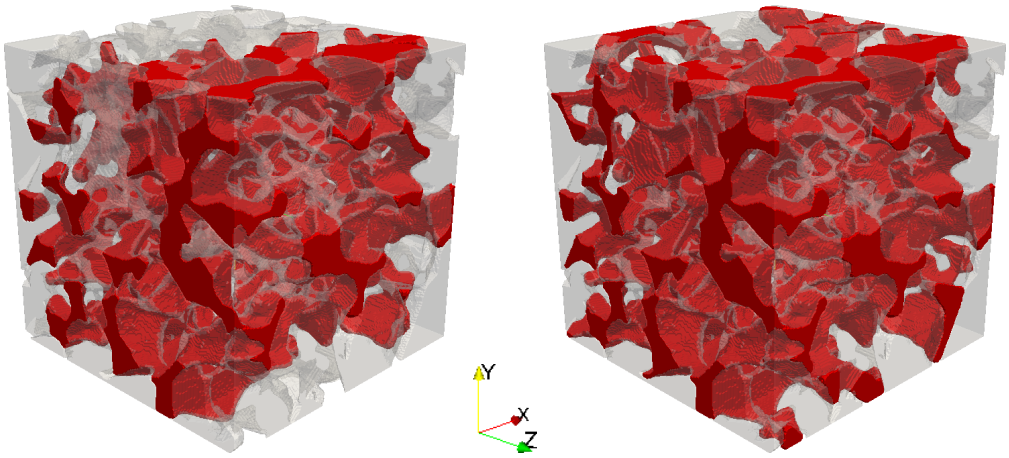

(c) $S_w = 24\%$ (d) $S_w = 11\%$

Figure 2.2: Simulated drainage stages in a 250^3 subset of the Fontainebleau sandstone. Grain phase is represented by the semi-transparent gray surface. Non-wetting phase (red surface in the figure) is entering the porous medium through the yz slice at $x = 0$.

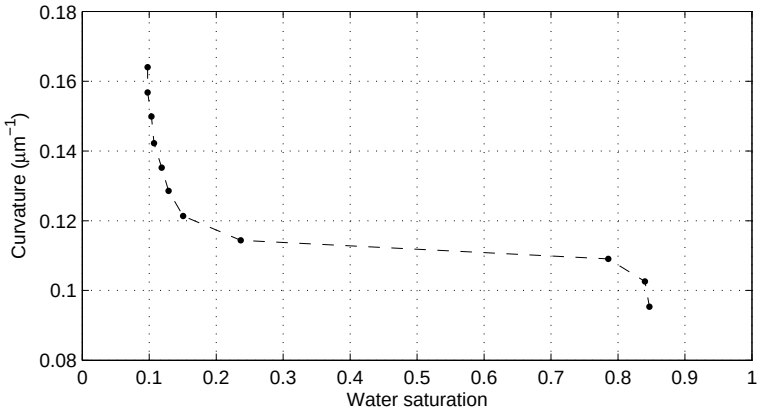

Figure 2.3: Curvature-saturation curve for the drainage simulation on Fontainebleau sandstone [61].

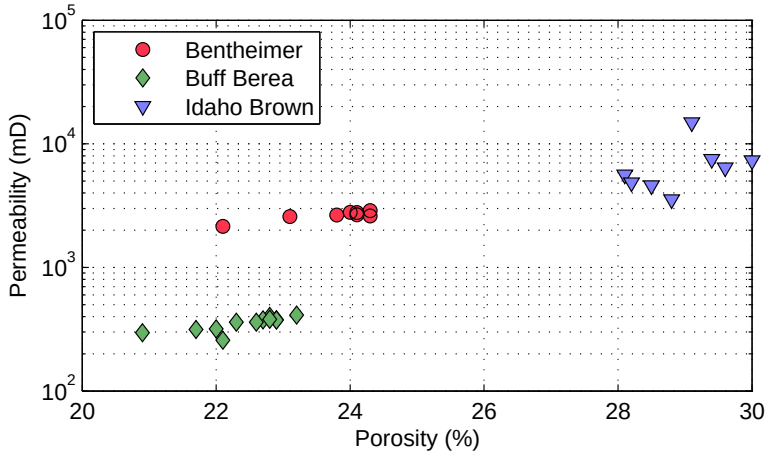

Figure 2.4: Routine core analysis for sister samples of Bentheimer, Buff Berea and Idaho Brown sandstones.

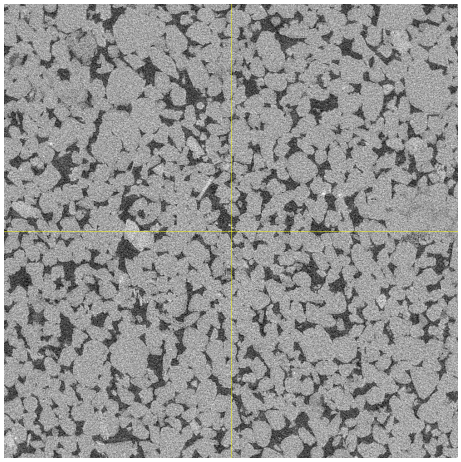

(a) xy slice at $z = 750$

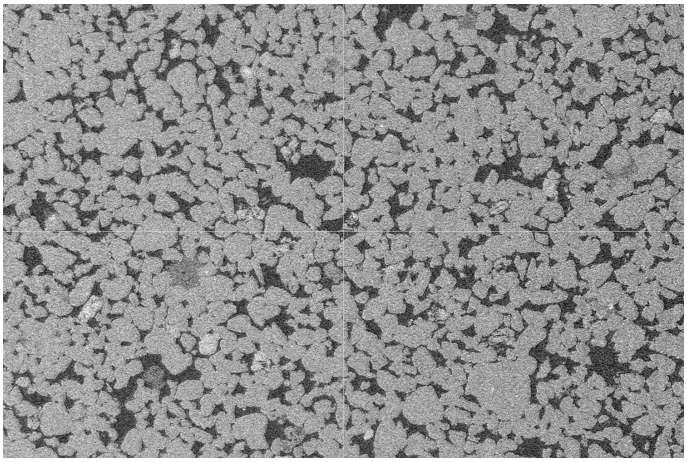

(b) yz slice at $x = 500$

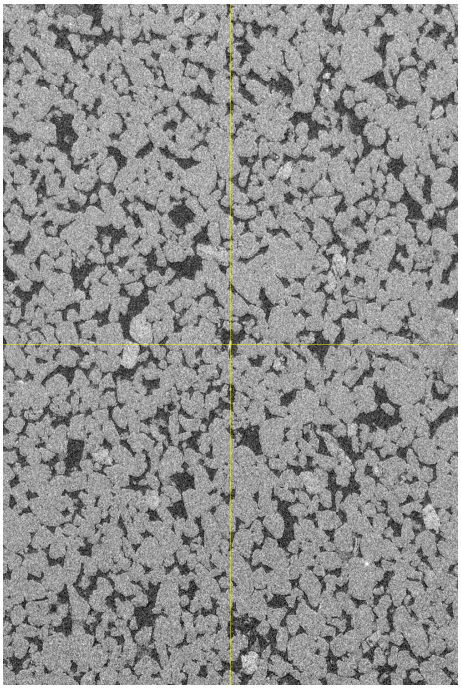

(c) xz slice at $y = 500$

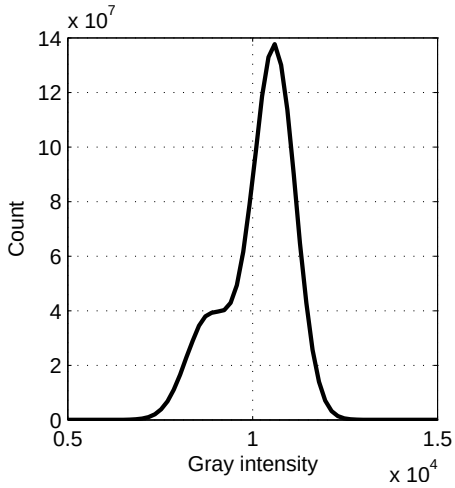

(d) Gray scale histogram

Figure 2.5: Cross-sections of the Bentheimer sandstone μ-CT image. Voxel size is equal to 5 μm and sample dimensions are $1000 \times 1000 \times 1500$ voxels. Coordinates x, y and z are counted in voxels in this figure.

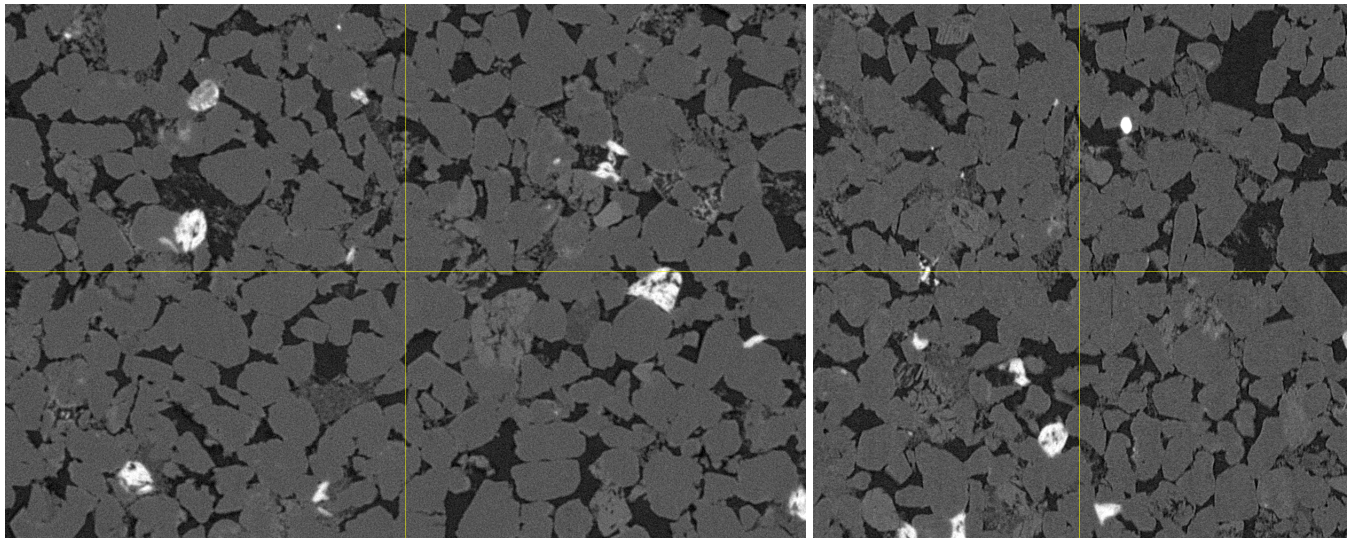

(a) xy slice at $z = 500$

(b) yz slice at $x = 750$

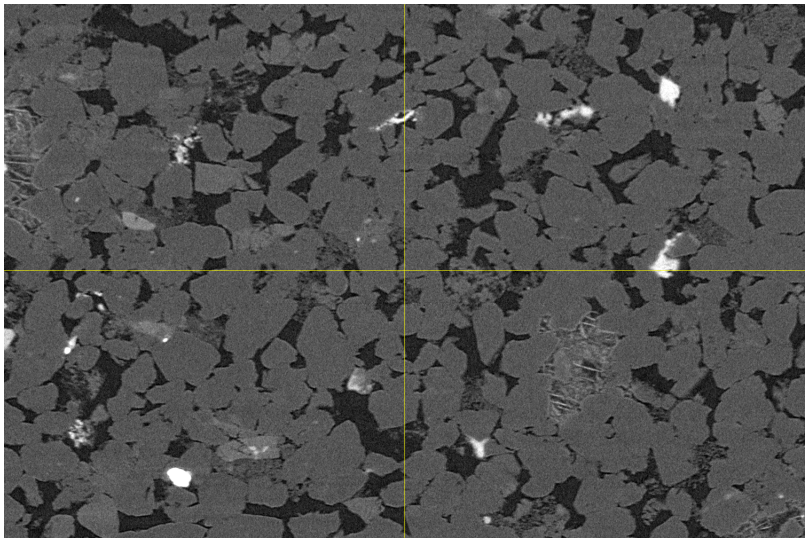

(c) xz slice at $y = 500$

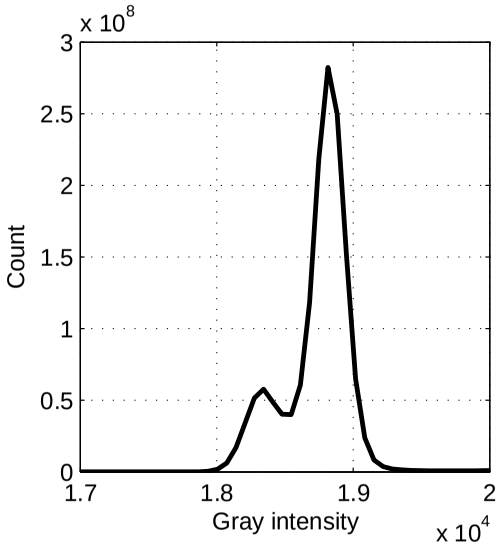

(d) Gray scale histogram

Figure 2.6: Cross-sections of the Buff Berea sandstone μ-CT image. Voxel size is equal to 2 μm and sample dimensions are $1500 \times 1000 \times 1000$ voxels. Coordinates x, y and z are counted in voxels in this figure.

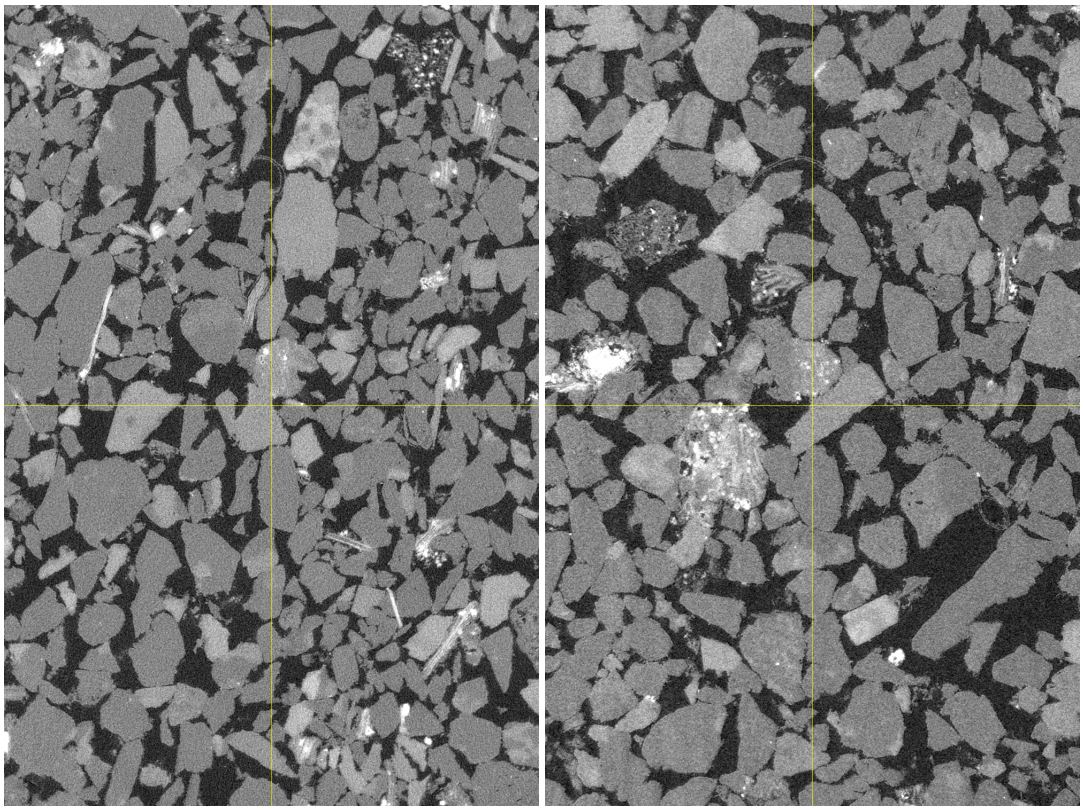

(a) xy slice at $z = 500$

(b) yz slice at $x = 500$

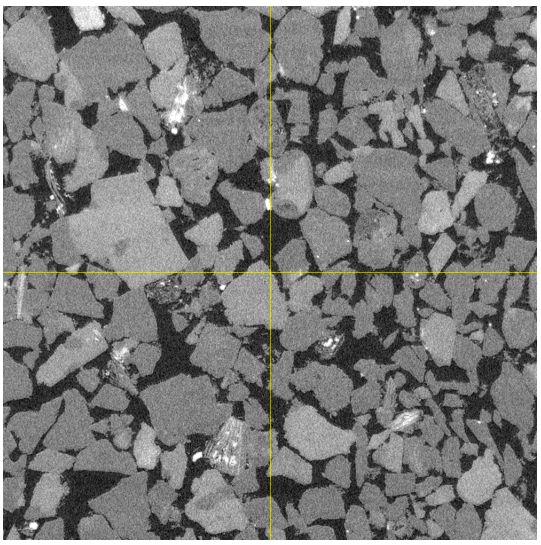

(c) xz slice at $y = 750$

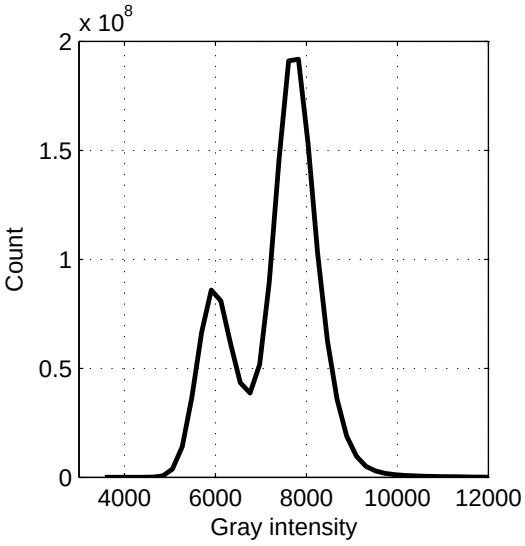

(d) Gray scale histogram

Figure 2.7: Cross-sections of the Idaho Brown sandstone μ-CT image. Voxel size is equal to 5 μm and sample dimensions are $1000 \times 1500 \times 1000$ voxels. Coordinates x, y and z are counted in voxels in this figure.

tistical tests on neighboring regions, merging them if the average intensities are considered similar enough. The algorithm is guided by an user input for the final number of regions.

Finally, a hard threshold on the merged image was applied to classify each voxel as a pore or a solid phase. Results will be shown in the next chapter.

Chapter 3: Results

3.1 Transport properties for Finney pack, Fontainebleau and dolomite

We first show results for pressure field and electric potential simulated. The left part of Figure 3.1 shows contour levels for the simulated pressure fields within each sample. These simulations were stopped when the relative error got 10^{-5} in order of magnitude. Qualitatively, the contour lines terminate at pore-grain interface in a perpendicular direction, indicating zero pressure variation normal to the interfaces, as required by the boundary conditions.

Computed pressure fields also represent the respective electric potentials for these samples. Recall that the model of electrically insulating grains and electrically conducting pores, as explained in section 2.1.3, reduces the equation and boundary conditions governing electric potential to the ones governing pressure. The right part of Figure 3.1 shows the electric flux across the sample in the z direction, calculated by the definition in equation (2.35). Effective conductivities with numerical uncertainties result from the mean value and the standard deviation on these curves.

The electric flux is fairly constant throughout the samples, except for the anomalous high values observed at the borders of the 3D domains, even negative within the first few slices. This boundary effect will enhance the uncertainty in the estimation of the volumetric properties and, for the velocity field calculation, the high pressure gradients at the borders will increase the volumetric flux in opposite directions, preventing the algorithm from finding a solution with small divergence.

Detailed investigation on the source of these inconsistent gradients is left for a future work. Presently we simply remove questionable boundary slices from consideration.

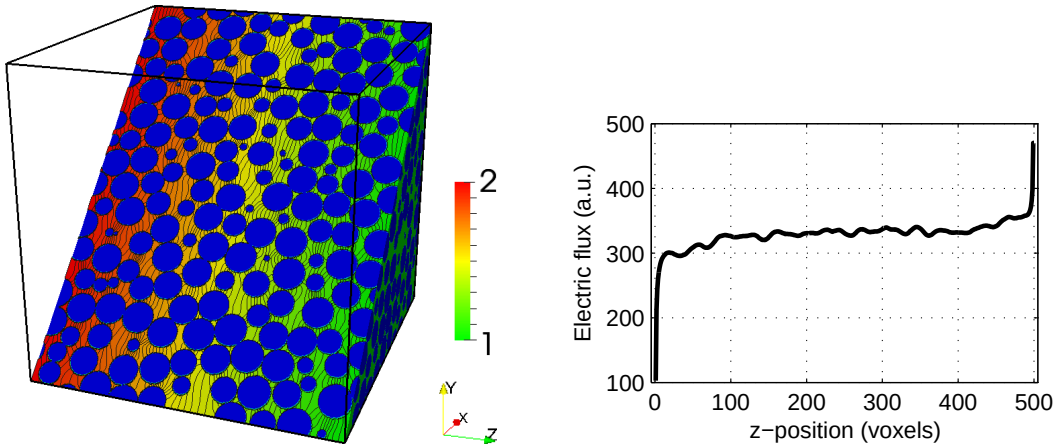

(a) Finney

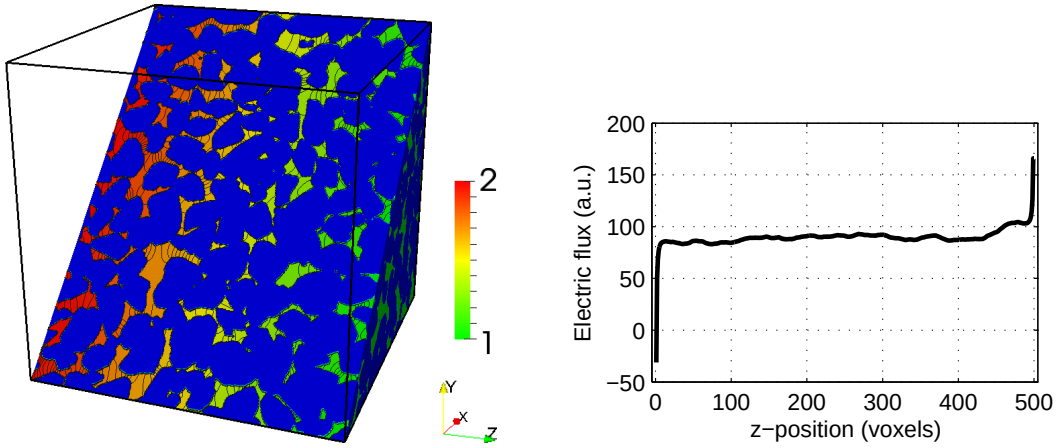

(b) Fontainebleau sandstone

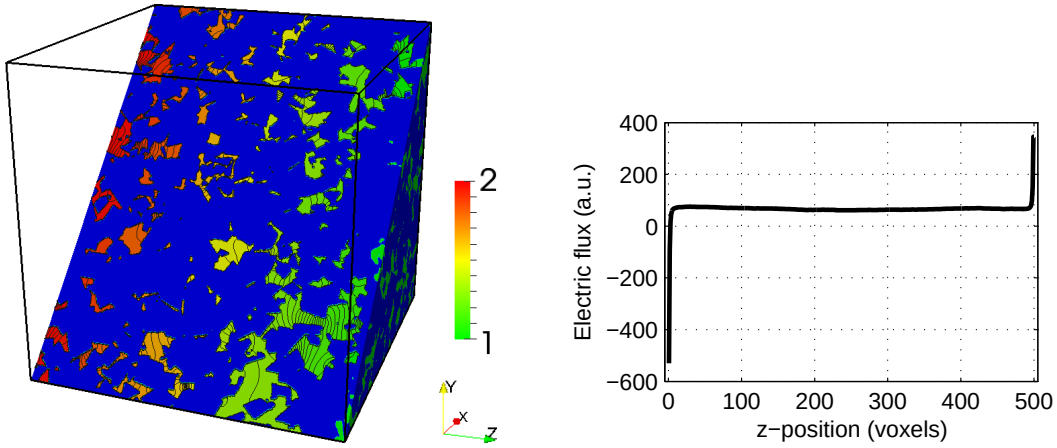

(c) Dolomite

Figure 3.1: Pressure/electric potential contour levels (left) and electric flux (right) resulting from the simulations. Numbers are presented in arbitrary units. Any consistent system of units can be used to scale the results, provided that distance is measured in micrometers.

Table 3.1: Results for simulation on the first group of samples. Permeability values are in darcy.

Sample	Porosity	$\hat{\sigma}$ simulated	$\hat{\sigma}$ literature	κ simulated	κ literature
Finney	0.3629	0.2208(30)	0.2186	22.92(90)	20
Fontainebleau	0.1947	0.0594(11)	0.0446	3.19(14)	3
Dolomite	0.2150	0.0454(31)	–	1.40(11)	0.9

Figure 3.2 shows the streamlines for the velocity fields and the respective volumetric flux distributions for each case.

Effective conductivity and absolute permeability are then calculated by equations (2.33) and (2.36), considering only this inner domain. The results can be compared with data in the literature. Effective conductivity for random sphere pack has been shown [71, 72] to be a function of sample porosity described by $\hat{\sigma} = \phi^{1.5}$. Permeability for this kind of porous medium has been accurately described by the Kozeny-Carman equation

$$\kappa = \frac{D_g^2 \phi^3}{72\tau(1-\phi)^2}, \tag{3.1}$$

where D_g is the grain diameter and $\tau = 5$ is the Kozeny constant for the sphere pack [2]. Doyen [73] reports the empirical correlation $\hat{\sigma} = \phi^{1.9}$ for a set of Fontainebleau sandstone cores in the same range of porosity as our sample. Permeability for sister samples of the Fontainebleau sandstone and the dolomite used in this project is reported by Shabro *et al.* [61]. Table 3.1 details the results, showing a very good agreement between simulations and literature values. It is also interesting to observe the higher values of permeability as a consequence of the higher interstitial velocity on Figure 3.2.

3.2 The effect of numerical diagenetic processes on electrical properties

A selection of samples after the dilation or erosion procedures described in section 2.3.2 are illustrated in Figure 3.3. Figure 3.4 shows the results for the electrical conductivity of the whole set. The eroded samples (higher porosity in the figure) behave as the power

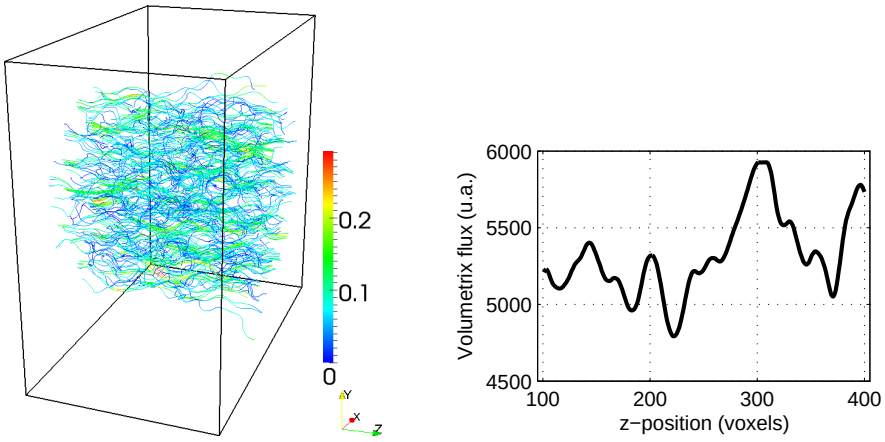

(a) Finney

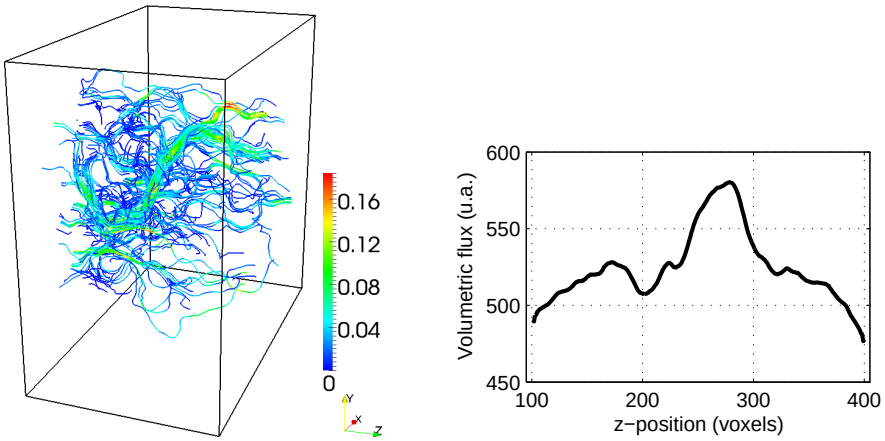

(b) Fontainebleau sandstone

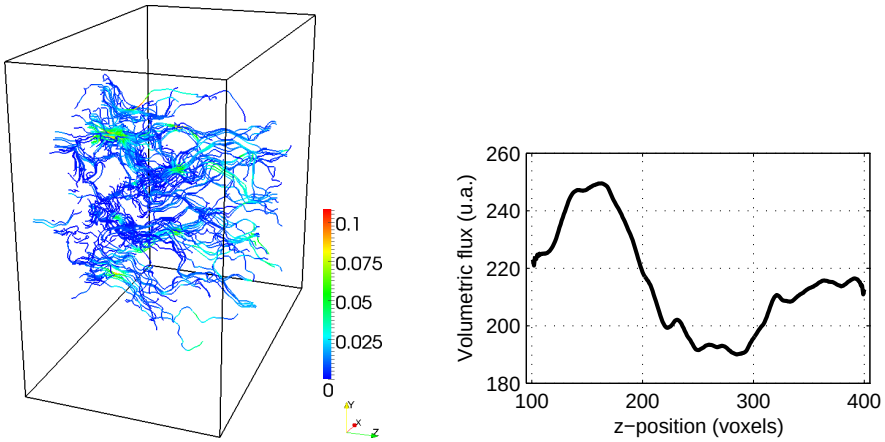

(c) Dolomite

Figure 3.2: Velocity streamlines (left) and volumetric flux (right) from the simulated velocity fields. Streamlines are colored by local velocity magnitude, whose units are consistent with the ones in Figure 3.1. Unit value is assigned to viscosity.

law expected for spherical inclusions in a conductive medium [71, 72]. Cemented samples (lower porosity), however, show gradual deviations from this behavior, and less conductive rocks result as a consequence of pore throats being blocked by the uniformly growing cement. The simulations agree closely with the work of Bryant and Pallatt [6], who calculated sphere pack conductivity by modeling a network of electrical resistors from the sample geometry.

3.3 Two-phase fluid displacement in the Fontainebleau sandstone

In the two-phase flow simulations we considered water as the wetting phase and oil as the non wetting phase. Electrical conductivity is calculated for each drainage step by setting the conductivity of the oil phase equal to zero.

With the assumption of capillary dominated fluid flow, each phase flows through a separate network of channels determined by the initial fluid distribution. We estimate effective permeability by assigning the voxels corresponding to one fluid phase to grain voxels and letting the other fluid phase flow in the remaining space. This approach has the advantage of using the same code designed to calculate absolute permeability, but also has the limitation of imposing zero velocity at the fluid-fluid interfaces. A more reasonable boundary condition would be the zero shear stress at fluid-fluid interfaces, since no viscous coupling between oil and water is usually assumed for flow at reservoir conditions [74]. Improvements for this specific limitation are left for future work.

Figure 3.5 shows the results. It is possible to see that, for this particular subsample, the invading oil phase quickly occupies the pore space. The percolation path for the water phase is disconnected after the third drainage step, when the water saturation suddenly drops from 0.79 to 0.23. Due to the size of the sample used, oil and water phases do not percolate simultaneously, as reflected in the relative permeability curves. Nevertheless, the results for the resistivity index seem to be at the trend defined by the experimental data

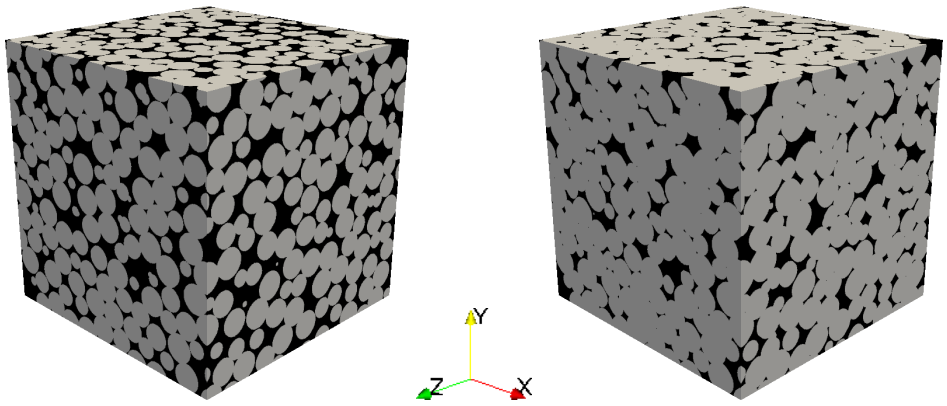

(a) Example of dilated samples

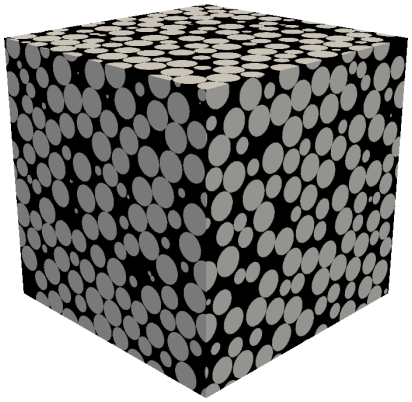

(b) Original pack

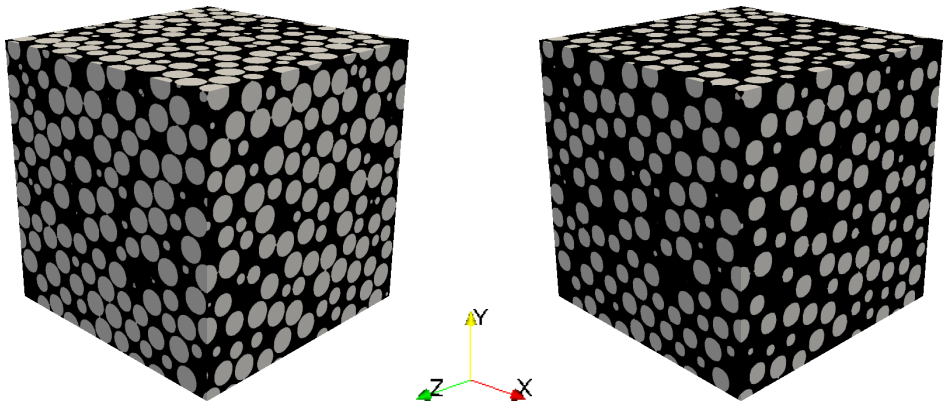

(c) Example of eroded samples

Figure 3.3: Dilation (numerical cementation) and erosion (numerical dissolution) operations on Finney pack.

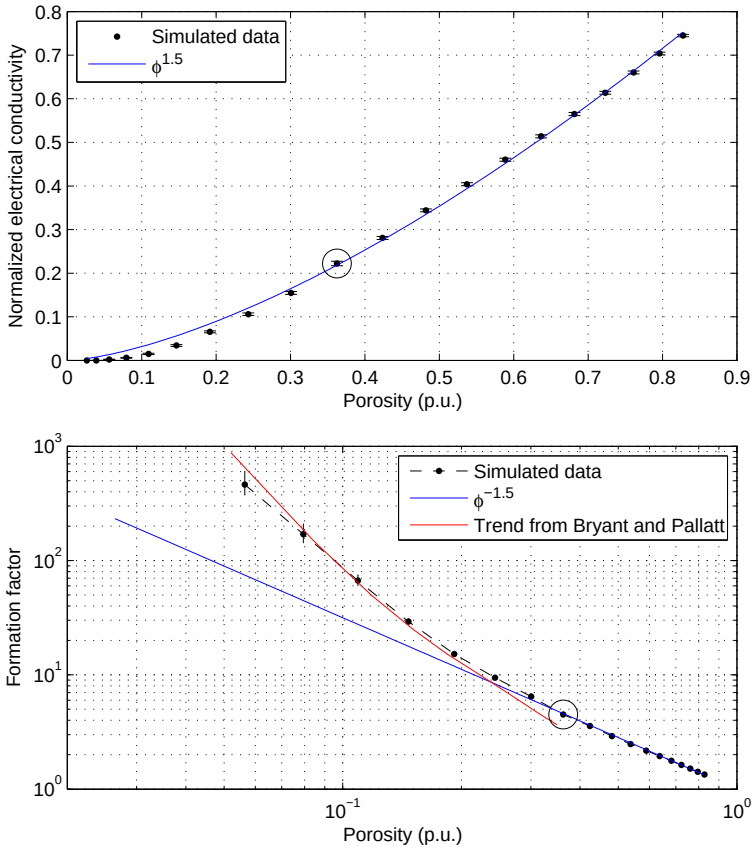

Figure 3.4: Effective conductivity for Finney dilated/eroded samples. Original Finney pack sample is marked by a circle. Cemented samples show agreement with trend from network model simulation from Bryant and Pallatt [6].

reported by Han *et al.* [18].

Figure 3.6 shows streamlines for representative water and oil velocity fields. Relative permeability for the oil phase shows a very good agreement with the lattice-Boltzman simulations on the same images by Shabro *et al.* [61]. The same is not true for the water relative permeability. The observed difference could be effect of trapped oil on the data used by that simulation. Discontinuous oil blobs in the middle of pore bodies significantly reduce the effective permeability of the water, but have no influence on the oil relative permeability, since those blobs do not contribute to the oil percolation path. It is possible to see the residual oil saturation on the reported drainage curve, reproduced again in Figure 3.7. Our data represents the beginning of the first drainage-imbibition cycle, where the oil is invading a porous medium 100% saturated with water.

3.4 Characterization of Bentheimer, Buff Berea and Idaho Brown sandstones

3.4.1 Segmentation

Representative slices for each step in the segmentation procedure are shown in figures 3.8, 3.9, and 3.10. The gray scale histograms show that the strategy of a median filter followed by the statistical region merging filter was sufficient as a preparation for thresholding in these good quality images.

Figure 3.11 shows the porosity values for each segmented subsample. Most of the data for Berea and Idaho Brown falls within three or four porosity units from the lab measured values. In contrast, porosity values for the segmented Buff Berea show a bigger discrepancy from the lab data. The choice of two-phase segmentation lumped together rock matrix and the intergrain clay minerals (see Figure 3.9(a)) as simply “grain phase”, lowering the value of porosity for the segmented image. Two-phase segmentation seems appropriate for the Bentheimer and Idaho Brown samples.

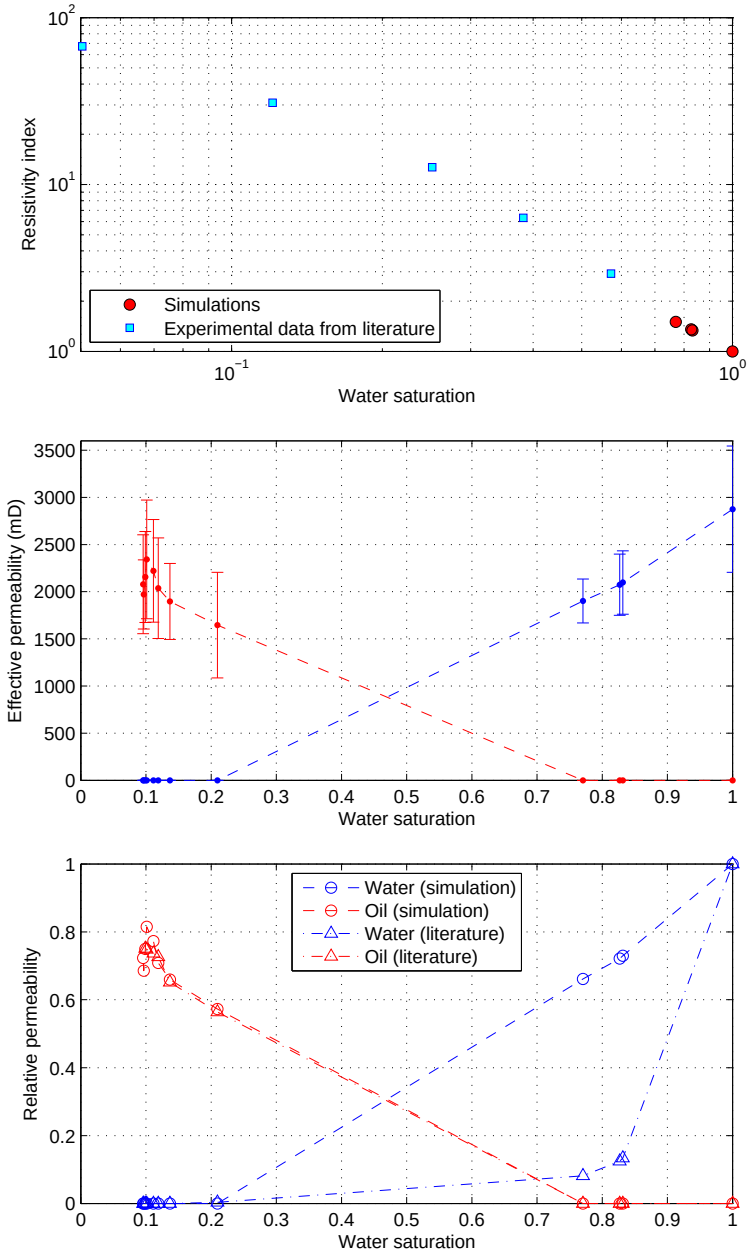

Figure 3.5: Simulation results for the set of drainage samples. Experimetal data for resistivity index is reported in [18]. Numerical error for the simulation on electrical conductivity is between five and ten percent. Data for relative permeability was published in [61].

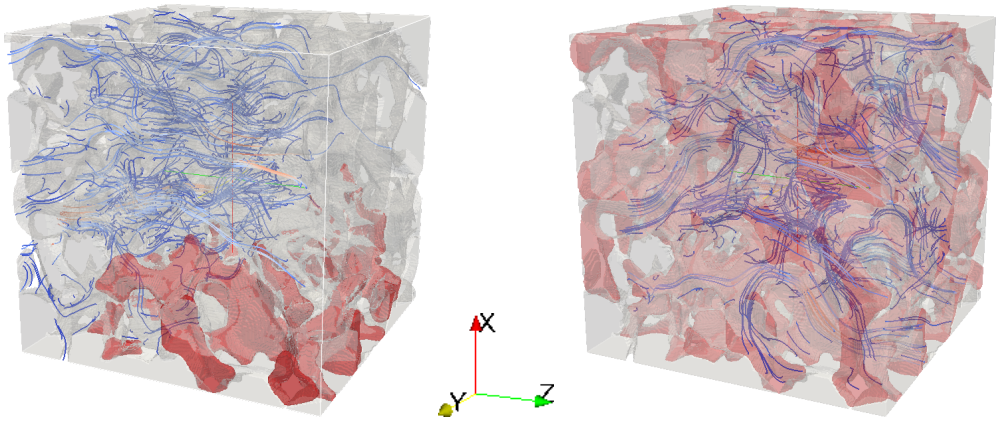

(a) $S_w = 79\%$ (b) $S_w = 11\%$

Figure 3.6: Velocity streamlines for two representative drainage states in the simulation for Fontainebleau sandstone. At early stages (a), oil phase is disconnected and at rest. At later stages (b), water phase is at rest due to the lack of a connected path. Oil is invading the pore space from the bottom in these figures (x direction) and the pressure gradient is applied parallel to z direction.

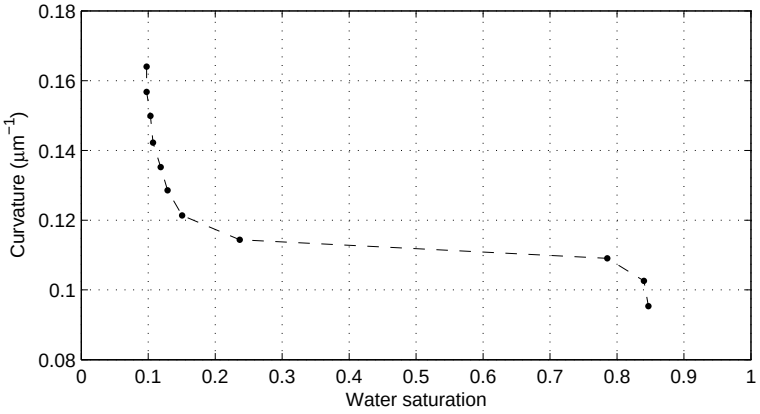

Figure 3.7: Curvature-saturation curve for the drainage simulation on the Fontainebleau sandstone [61].

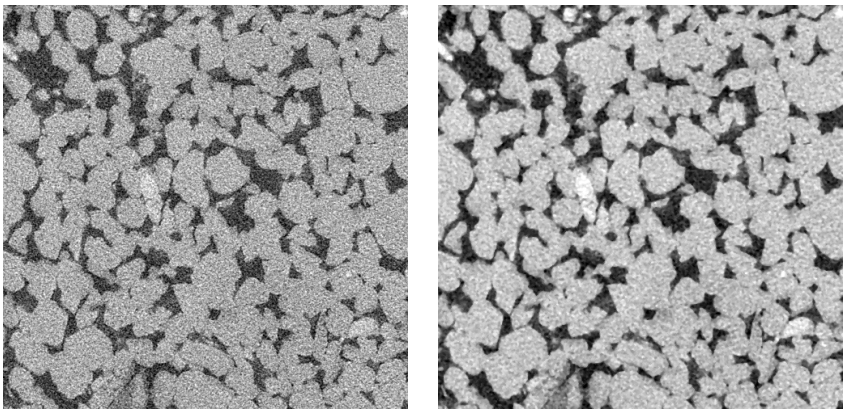

(a) Original slice

(b) After median filter

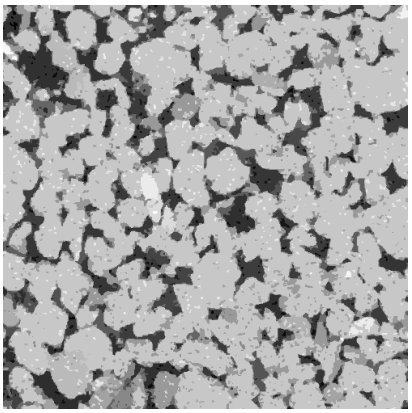

(c) After region merging

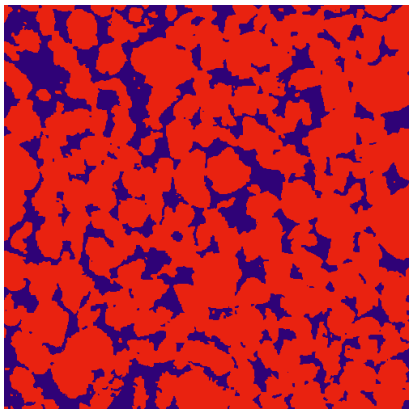

(d) After thresholding

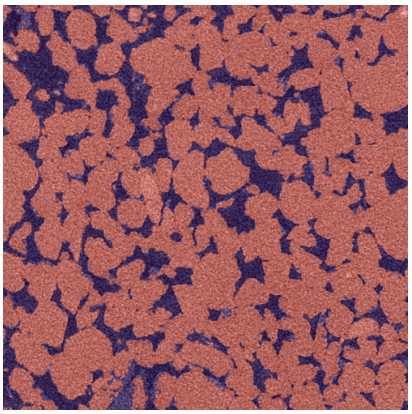

(e) Comparison original–thresholded

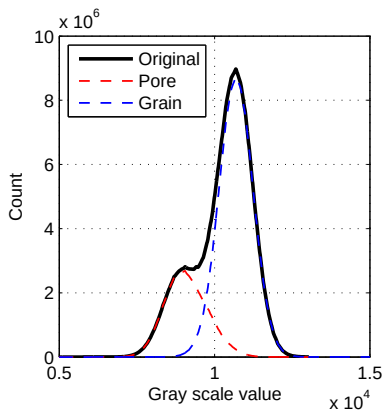

(f) Gray scale histogram

Figure 3.8: Example of segmentation result for one of the Bentheimer sandstone subsamples. Blue represents pore space and red represents solid space. Slices have 500×500 voxels and voxel size is equal to 5 μm.

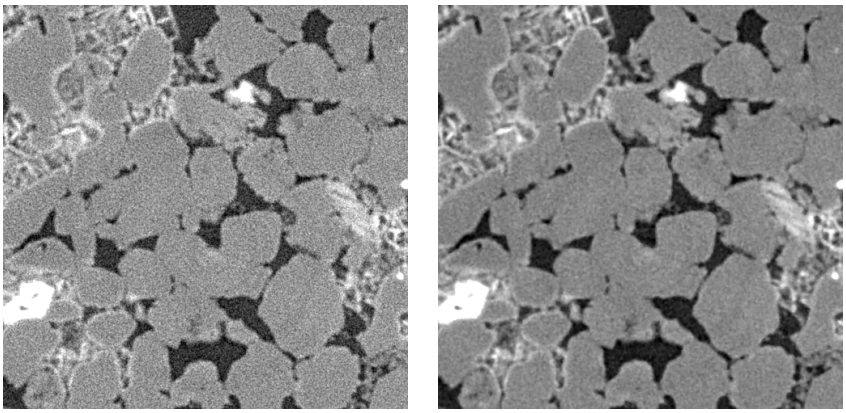

(a) Original slice

(b) After median filter

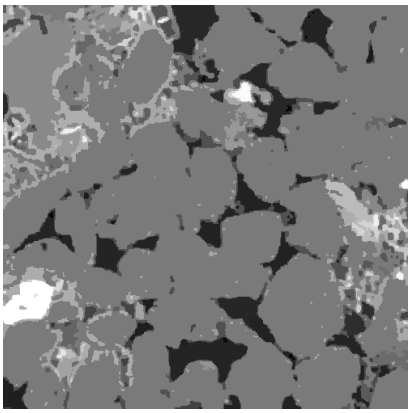

(c) After region merging

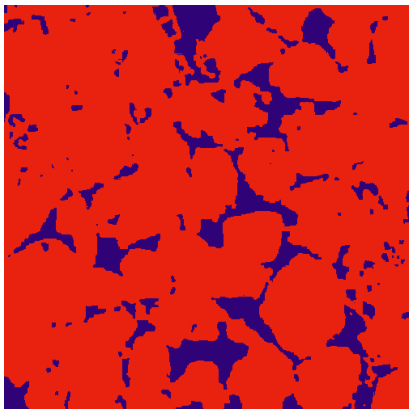

(d) After thresholding

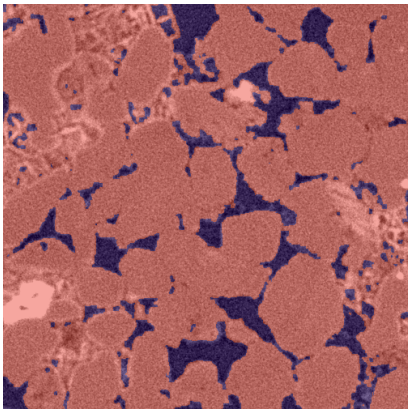

(e) Comparison original–thresholded

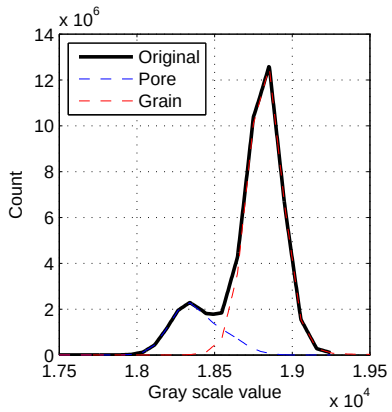

(f) Gray scale histogram

Figure 3.9: Example of segmentation result for one of the Buff Berea sandstone subsamples. Blue represents pore space and red represents solid space. Slices have 500×500 voxels and voxel size is equal to 2 μm.

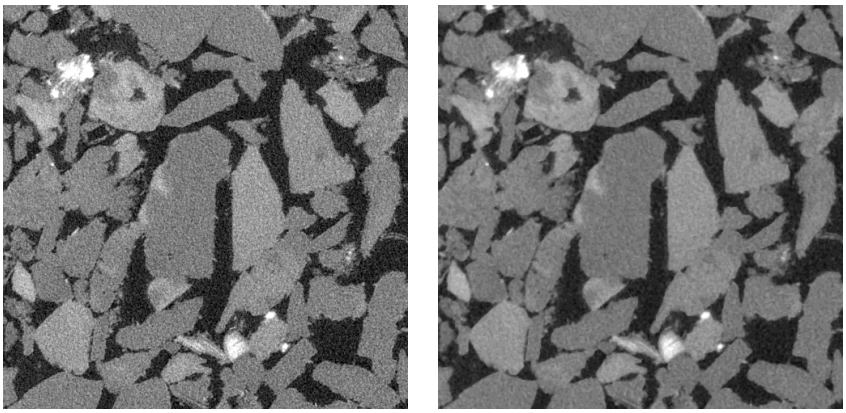

(a) Original slice

(b) After median filter

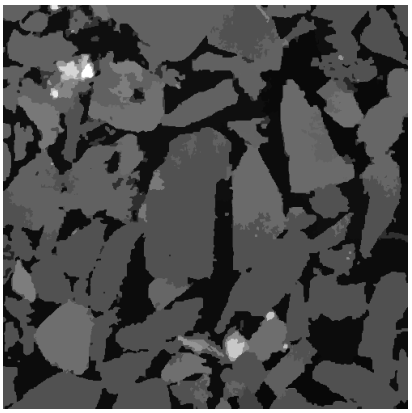

(c) After region merging

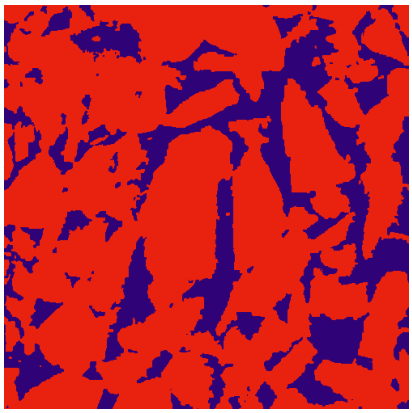

(d) After thresholding

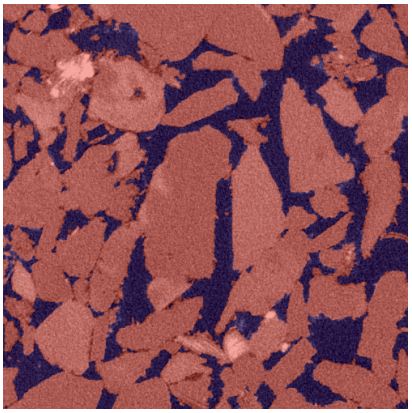

(e) Comparison original–thresholded

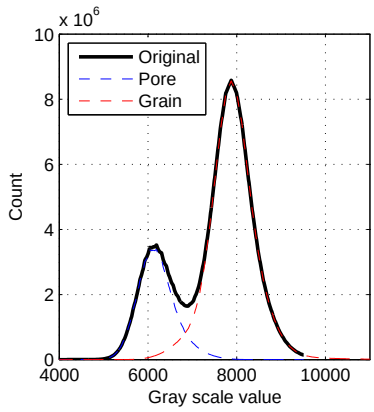

(f) Gray scale histogram

Figure 3.10: Example of segmentation result for one of the Idaho Brown sandstone subsamples. Blue represents pore space and red represents solid space. Slices have 500×500 voxels and voxel size is equal to 5 μm.

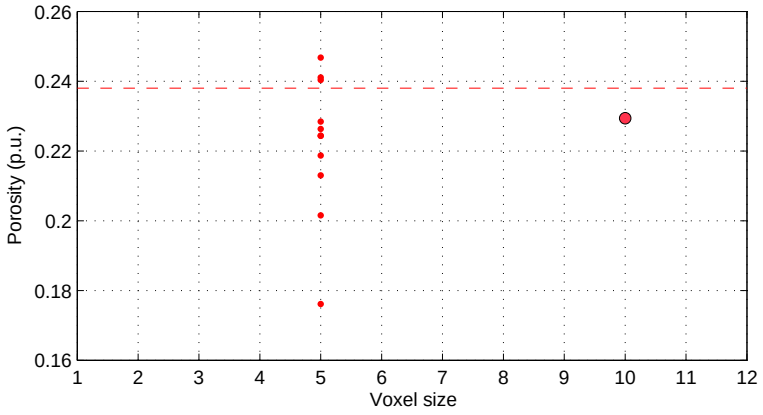

(a) Bentheimer

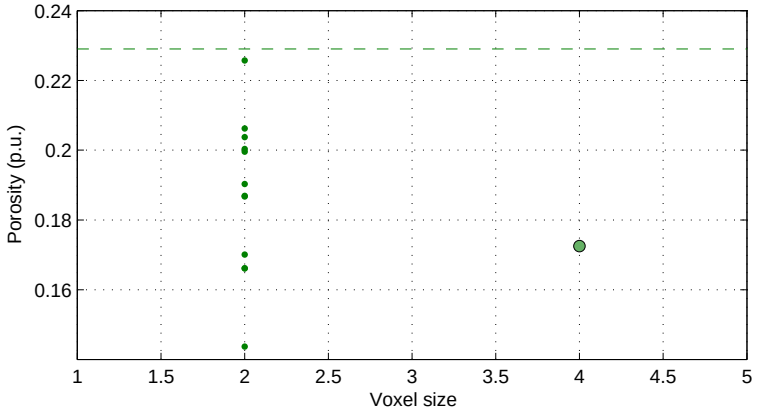

(b) Buff Berea

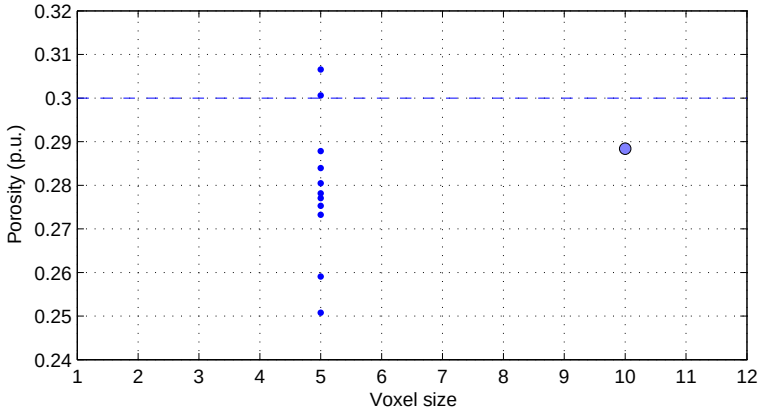

(c) Idaho Brown

Figure 3.11: Porosity results for the twelve 500^3 subsamples (dots) and the upscaled full image (circle) of Bentheimer, Buff Berea and Idaho Brown data sets. Dashed line represents laboratory measurement on the full plug.

3.4.2 Transport properties

Figure 3.12 shows the results for the electrical conductivity simulation. The three sets of data show a trend that could be reasonably described by Archie's model with appropriate fitting parameters, and also captures the experimental value measured on the original plug. This trend is well defined for the Bentheimer subsamples, the group with more scattered values for porosity. Buff Berea simulations also show good agreement with lab data, suggesting that the clay minerals play a minor role in electrical conductivity for this sample. A quantitative investigation by segmenting the clay minerals as a separate phase is needed to confirm this hypothesis. The Idaho Brown results show the best agreement with laboratory data (note the different scales for each plot), probably due to the closer values of porosity. Finally, we did not observe any influence of sample size or resolution for the group of studied samples, since the values for electrical conductivity for the low resolution versions fall on the same trend.

Figure 3.13 shows the corresponding results for absolute permeability. These results vary within one order of magnitude, and are systematically higher than the experimentally measured absolute permeability on the full plug. Again, it is possible to notice a weak trend relating porosity and permeability from the simulations. The trend is better defined for the Bentheimer sandstone, while it is very weak on the Idaho results. These behavior can be explained by grain size distribution. Each small subsample probes a slightly different pore geometry on the Bentheimer sandstone, but the poor grain sorting for the Idaho Brow causes the corresponding subsamples to probe very different pore geometries.

Also, no matter the voxel length, there are likely pore throats that are poorly resolved (i.e., less than five voxels in cross-section). Those affect convergence for velocity field, but would have minor effect on the electric field. Due to the no-slip boundary condition for the viscous flow, small throats will effectively block the flow if there are not enough voxels to describe the velocity field within those throats. Lack of numerical convergence

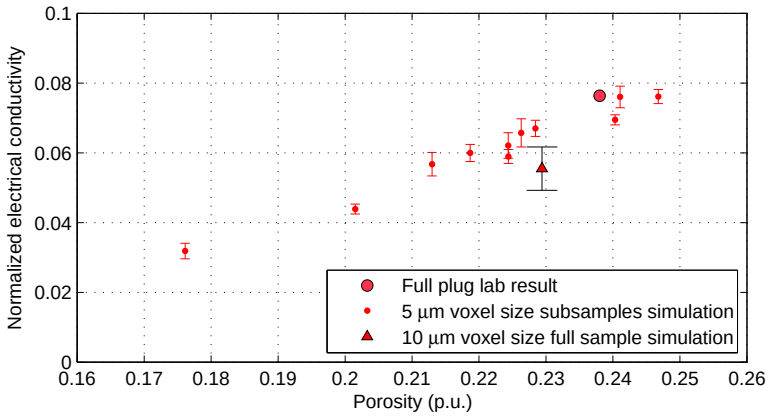

(a) Bentheimer sandstone

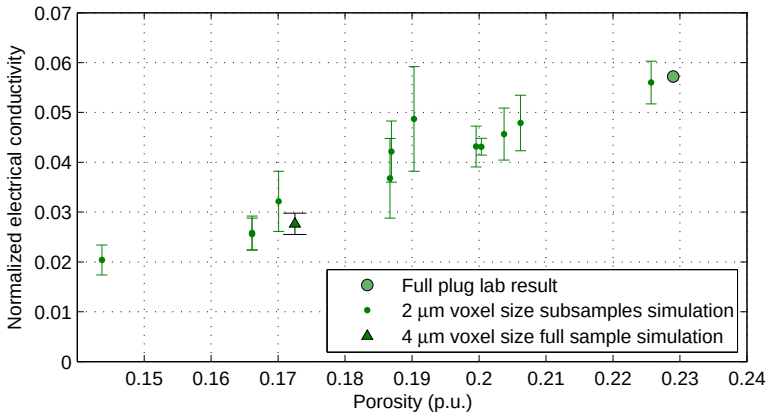

(b) Buff Berea sandstone

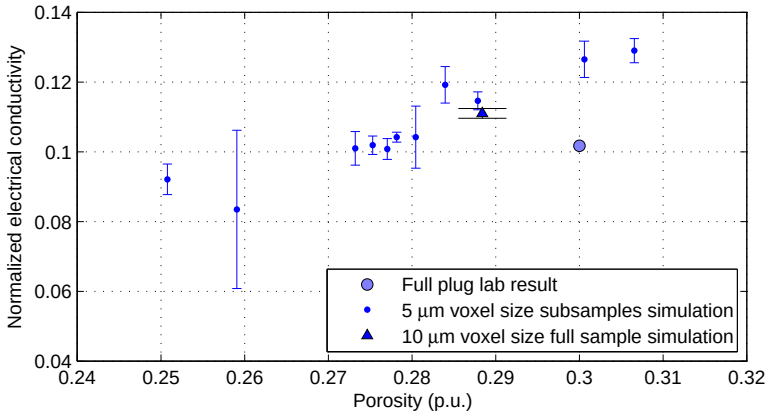

(c) Idaho Brown sandstone

Figure 3.12: Results from electrical conductivity simulations.

could explain why most of the permeability simulations are higher than the experimental value while the simulations for electrical conductivity succeed in getting the correct trend.

Finally, the presence of small throats will enhance the abnormal border effects for the pressure gradient. A stronger flux will result if the gradient at the open boundaries is not treated properly, resulting in these high values for permeability. Confirmation of this hypothesis requires a detailed investigation on each one of the pressure and velocity fields, since the strategy of removing boundary slices was automated due to the number of simulations.

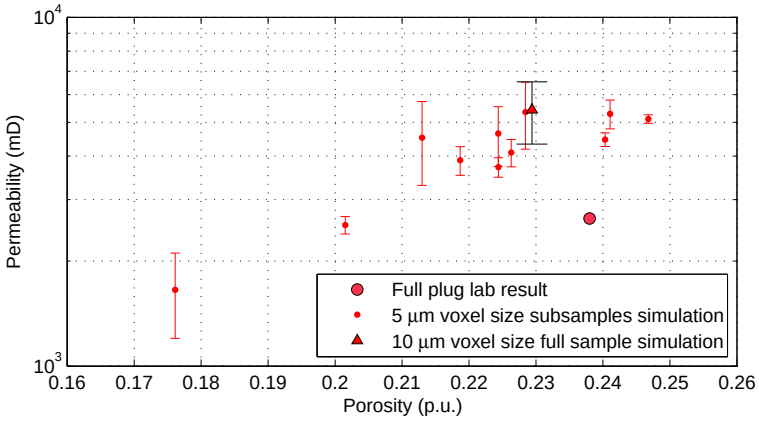

(a) Bentheimer sandstone

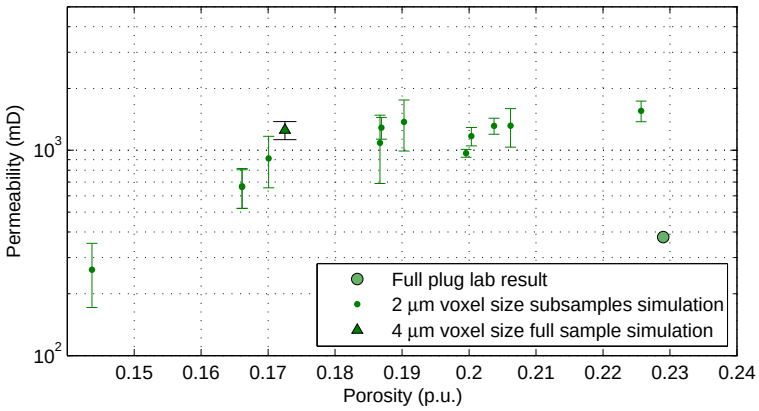

(b) Buff Berea sandstone

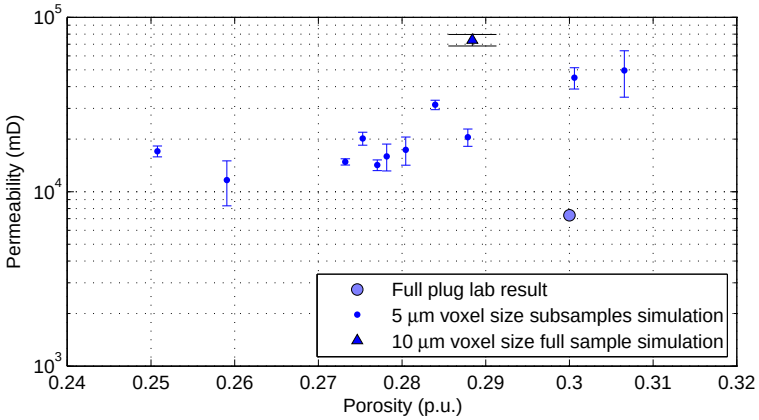

(c) Idaho Brown sandstone

Figure 3.13: Results from absolute permeability simulations.

Chapter 4: Conclusion

We assessed the quality of the results based on over 70 simulations shown in the last chapter. Comparison using benchmark samples revealed excellent agreement between the transport properties from our simulations and from the literature. However, tests on outcrop sandstone samples resulted in systematically larger values for permeability, which needs to be further investigated.

Besides having a good estimate of the porous medium effective properties, the finite differences method also generates a detailed description of pressure, electric, and velocity fields. This information can be used in the future to investigate the relation between the pore space and the macroscopic property in complex rocks, where simplified models are not available. The possibility of handling spatially varying electrical conductivity will be valuable for predicting electrical properties of rocks with multiscale pore systems, e.g. certain carbonates and tight gas sandstones.

Tikhonov regularization showed to be a reliable tool for maintaining low divergence in the solution of Stokes equation with zero Neumann boundary conditions. This constitutes an alternative and effective way to use finite differences to calculate the velocity field and estimate the hydraulic permeability, without any additional simplification or forced boundary condition. Nevertheless, we need to find an automatic way to set the regularization parameter for our specific formulation.

The main limitation observed so far is the anomalous values for gradient fields at the open boundaries, whose source is still unknown, and may be the cause for the high permeability values on Bentheimer, Buff Berea and Idaho Brown sandstones. In addition, the speed of convergence for the velocity field can always be improved.

Besides investigating all the aforementioned technical limitations, our future phys-

ical extensions include the investigation of complex samples as carbonate rocks with multiscale porosity and implementation of multiphase fluid flow.

References

[1] Archie, G. E. The electrical resistivity log as an aid in determining some reservoir characteristics. *Trans. AIMe*, 146(99):54–62, 1942.

[2] Peters, E. J. *Advanced Petrophysics: geology, porosity, absolute permeability, heterogeneity, and geostatistics*, volume 1. Greenleaf Book Group, 2012.

[3] Finney, J. Random packings and the structure of simple liquids. I. The geometry of random close packing. *Proceedings of the Royal Society of London. A. Mathematical and Physical Sciences*, 319(1539):479–493, 1970.

[4] Ellis, M. H, Sinha, M. C, Minshull, T. A, Sothcott, J, and Best, A. I. An anisotropic model for the electrical resistivity of two-phase geologic materials. *Geophysics*, 75(6):E161–E170, 2010.

[5] Jin, G, Torres-Verdín, C, and Toumelin, E. Comparison of NMR simulations of porous media derived from analytical and voxelized representations. *Journal of Magnetic Resonance*, 200(2):313–320, 2009.

[6] Bryant, S and Pallatt, N. Predicting formation factor and resistivity index in simple sandstones. *Journal of Petroleum Science and Engineering*, 15(2):169–179, 1996.

[7] Blunt, M. J, Bijeljic, B, Dong, H, Gharbi, O, Iglauer, S, Mostaghimi, P, Paluszny, A, and Pentland, C. Pore-scale imaging and modelling. *Advances in Water Resources*, 51:197–216, 2013.

[8] Wildenschild, D and Sheppard, A. P. X-ray imaging and analysis techniques for quantifying pore-scale structure and processes in subsurface porous medium systems. *Advances in Water Resources*, 51:217–246, 2013.

[9] Bird, R. B, Stewart, W. E, and Lightfoot, E. N. *Transport Phenomena*. Wiley New York, 2 edition, 1960.

[10] Tu, J, Yeoh, G. H, and Liu, C. *Computational fluid dynamics: a practical approach*. Butterworth-Heinemann, 2007.

[11] Shabro, V, Torres-Verdn, C, Javadpour, F, and Sepehrnoori, K. Finite-difference approximation for fluid-flow simulation and calculation of permeability in porous media. *Transport in Porous Media*, 94:775–793, 2012.

[12] Whitaker, S. Flow in porous media I: A theoretical derivation of Darcy's law. *Transport in porous media*, 1(1):3–25, 1986.

[13] Willhite, G. P. *Waterflooding*. Society of Petroleum Engineers, Richardson, TX, 1986.

[14] Morrow, N. R. Physics and thermodynamics of capillary action in porous media. *Industrial & Engineering Chemistry*, 62(6):32–56, 1970.

[15] Jackson, J. D and Jackson, J. D. *Classical Electrodynamics*, volume 3. Wiley New York, 1962.

[16] Kennedy, W. D and Herrick, D. C. Conductivity models for Archie rocks. *Geophysics*, 77(3):WA109–WA128, 2012.

[17] Devarajan, S, Toumelin, E, Torres-Verdín, C, Thomas, E, and Petrophysics, B. Pore-scale analysis of the Waxman-Smits shaly sand conductivity model. In *SPWLA 47th Annual Logging Symposium*, pages 1–9, 2006.

[18] Han, M, Youssef, S, Rosenberg, E, Fleury, M, and Levitz, P. Deviation from Archie's law in partially saturated porous media: wetting film versus disconnectedness of the conducting phase. *Physical Review E*, 79(3):031127, 2009.

[19] Zhan, X, Schwartz, L. M, Toksöz, M. N, Smith, W. C, and Morgan, F. D. Pore-scale modeling of electrical and fluid transport in berea sandstone. *Geophysics*, 75(5):F135–F142, 2010.

[20] Knackstedt, M, Arns, C, Sheppard, A, Senden, T, Sok, R, Cinar, Y, Pinczewski, W, Ioannidis, M, and Padhy,. Archies exponents in complex lithologies derived from 3d digital core analysis. In *SPWLA 48th Annual Logging Symposium held in Austin, Texas, United States*, 2007.

[21] Knackstedt, M. A, Sok, R. M, Sheppard, A. P, Latham, S. J, Madadi, M. A, Varslot, T. A, Arns, C. H, Bachle, G. A, and Eberli, G. A. Probing pore systems in carbonates: correlations to petrophysical properties. In *the Proceedings of the SPWLA 49th Annual Logging Symposium. Austin: Society of Petrophysicists and Well Log Analysts*, 2008.

[22] Arns, C, Bauget, F, Limaye, A, Sakellariou, A, Senden, T, Sheppard, A, Sok, R. M, Pinczewski, V, Bakke, S, Berge, L. I, Oren, P. E, and Knackstedt, M. A. Pore scale characterization of carbonates using X-ray microtomography. *Spe Journal*, 10(4):475–484, 2005.

[23] Yanici, S, Arns, J.-Y, Cinar, Y, Pinczewski, W, and Arns, C. Percolation effects of grain contacts in partially saturated sandstones: deviations from Archie's Law. *Transport in porous media*, 96(3):457–467, 2013.

[24] Khalili, A. D, Yanici, S, Cinar, Y, and Arns, C. H. Formation factor for heterogeneous carbonate rocks using multi-scale Xray-CT images. *Journal of Engineering Research*, 1(2):5–28, 2013.

[25] Flannery, B. P, Deckman, H. W, Roberge, W. G, and D'AMICO, K. L. Three-dimensional X-ray microtomography. *Science*, 237(4821):1439–1444, 1987.

[26] Cnudde, V and Boone, M. High-resolution X-ray computed tomography in geosciences: a review of the current technology and applications. *Earth-Science Reviews*, 123:1–17, 2013.

[27] Iassonov, P, Gebrenegus, T, and Tuller, M. Segmentation of X-ray computed tomography images of porous materials: a crucial step for characterization and quantitative analysis of pore structures. *Water resources research*, 45(9), 2009.

[28] Schlüter, S, Sheppard, A, Brown, K, and Wildenschild, D. Image processing of multiphase images obtained via X-ray microtomography: a review. *Water Resources Research*, 50(4):3615–3639, 2014.

[29] Bryant, S and Blunt, M. Prediction of relative permeability in simple porous media. *Physical Review A*, 46:2004–2011, Aug 1992.

[30] Bryant, S. L, King, P. R, and Mellor, D. W. Network model evaluation of permeability and spatial correlation in a real random sphere packing. *Transport in Porous Media*, 11(1):53–70, 1993.

[31] Blunt, M. J. Flow in porous media–pore-network models and multiphase flow. *Current opinion in colloid & interface science*, 6(3):197–207, 2001.

[32] Blunt, M. J, Jackson, M. D, Piri, M, and Valvatne, P. H. Detailed physics, predictive capabilities and macroscopic consequences for pore-network models of multiphase flow. *Advances in Water Resources*, 25(8):1069–1089, 2002.

[33] Mousavi, M. A and Bryant, S. L. Connectivity of pore space as a control on two-phase flow properties of tight-gas sandstones. *Transport in porous media*, 94(2):537–554, 2012.

[34] Mehmani, A, Prodanović, M, and Javadpour, F. Multiscale, multiphysics network modeling of shale matrix gas flows. *Transport in porous media*, 99(2):377–390, 2013.

[35] Ladd, A. J. Numerical simulations of particulate suspensions via a discretized Boltzmann equation. Part 1. Theoretical foundation. *Journal of Fluid Mechanics*, 271:285–309, 1994.

[36] Ladd, A. J. Numerical simulations of particulate suspensions via a discretized Boltzmann equation. Part 2. Numerical results. *Journal of Fluid Mechanics*, 271:311–339, 1994.

[37] Arns, C. H, Knackstedt, M. A, Pinczewski, W. V, and Martys, N. S. Virtual permeametry on microtomographic images. *Journal of Petroleum Science and Engineering*, 45(1):41–46, 2004.

[38] Andrä, H, Combaret, N, Dvorkin, J, Glatt, E, Han, J, Kabel, M, Keehm, Y, Krzikalla, F, Lee, M, Madonna, C, Marsh, M, Mukerji, T, Saenger, E. H, Sain, R, Saxena, N, Ricker, S, Wiegmann, A, and Zhan, X. Digital Rock Physics Benchmarks–Part II: Computing effective properties. *Computers & Geosciences*, 50:33–43, 2013.

[39] Knackstedt, M. A, Latham, S, Madadi, M, Sheppard, A, Varslot, T, and Arns, C. Digital rock physics: 3D imaging of core material and correlations to acoustic and flow properties. *The Leading Edge*, 28(1):28–33, 2009.

[40] Porter, M. L, Schaap, M. G, and Wildenschild, D. Lattice-Boltzmann simulations of the capillary pressure–saturation–interfacial area relationship for porous media. *Advances in Water Resources*, 32(11):1632–1640, 2009.

[41] Barth, W. L and Carey, G. F. On a boundary condition for pressure-driven laminar flow of incompressible fluids. *International journal for numerical methods in fluids*, 54(11):1313–1325, 2007.

[42] Nordström, J, Mattsson, K, and Swanson, C. Boundary conditions for a divergence free velocity-pressure formulation of the navier-stokes equations. *Journal of Computational Physics*, 225:874–890, 2007.

[43] Ol'Shanskii, M and Staroverov, V. On simulation of outflow boundary conditions in finite difference calculations for incompressible fluid. *International Journal for Numerical Methods in Fluids*, 33(4):499–534, 2000.

[44] Silin, D and Patzek, T. A pore-scale model of two-phase flow in water-wet rock. *Lawrence Berkeley National Laboratory*, 2009.

[45] Moshkin, N and Yambangwai, D. On numerical solution of the incompressible navier-stokes equations with static or total pressure specified on boundaries. *Mathematical Problems in Engineering*, 2009, 2009.

[46] Knackstedt, M, Arns, C, Sheppard, A, Senden, T, Sok, R, Cinar, Y, Olafuyi, A, Pinczewski, W, Padhy, G, and Ioannidis, M. Pore scale analysis of electrical resistivity in complex core material. In *International Symposium of the Society of Core Analysts held in Calgary, Canada*, pages 10–12, 2007.

[47] Wiegmann, A and Zemitis, A. *EJ-HEAT: A fast explicit jump harmonic averaging solver for the effective heat conductivity of composite materials*. Fraunhofer-Institut für Techno-und Wirtschaftsmathematik, Fraunhofer (ITWM), 2006.

[48] Yue, W, Tao, G, Liu, D, and Yang, W. Numerical simulation of non-archie electrophysical property of saturated rock with lattice boltzmann method. *Petroleum Science*, 6(1):24–28, 2009.

[49] Dvorkin, J, Derzhi, N, Diaz, E, and Fang, Q. Relevance of computational rock physics. *Geophysics*, 76(5):E141–E153, 2011.

[50] Arns, C. H, Knackstedt, M. A, Pinczewski, M. V, and Lindquist, W. Accurate estimation of transport properties from microtomographic images. *Geophysical Research Letters*, 28(17):3361–3364, 2001.

[51] Arns, C. An analysis of NMR-permeability scaling rules by numerical MRI. In *48th Annual Logging Symposium*. Society of Petrophysicists and Well-Log Analysts, 2007.

[52] Arns, C, Sheppard, A. P, Sok, R. M, and Knackstedt, M. NMR petrophysical predictions on digitized core images. *Petrophysics*, 48(3):202, 2007.

[53] Arns, C and Meleán, Y. Accurate simulation of NMR responses of mono-mineralic carbonate rocks using Xray-CT Images. In *SPWLA 50th Annual Logging Symposium*, 2009.

[54] Toumelin, E. *Pore-Scale Petrophysical Models for the Simulation and Combined Interpretation of Nuclear Magnetic Resonance and Wide-Band Electromagnetic Measurements of Saturated Rocks*. The University of Texas at Austin, 2006.

[55] Silin, D and Patzek, T. Pore space morphology analysis using maximal inscribed spheres. *Physica A: Statistical Mechanics and its Applications*, 371(2):336–360, 2006.

[56] Hilpert, M and Miller, C. T. Pore-morphology-based simulation of drainage in totally wetting porous media. *Advances in Water Resources*, 24(3):243–255, 2001.

[57] Knackstedt, M. A, Sok, R, and Adrian, S. 3D pore scale characterisation of carbonate core: relating pore types and interconnectivity to petrophysical and multiphase flow properties. In *International Petroleum Technology Conference*. International Petroleum Technology Conference, 2007.

[58] Ghous, A, Bauget, F, Arns, C, Sakellariou, A, Senden, T, Sheppard, A, Sok, R, Pinczewski, W, Harris, R, Beck, G, and Knackstedt, M. Resistivity and permeability anisotropy measured in laminated sands via digital core analysis. In *paper VVV, 46th SPWLA annual logging symposium*, 2005.

[59] Prodanović, M and Bryant, S. L. A level set method for determining critical curvatures for drainage and imbibition. *Journal of colloid and interface science*, 304(2):442–458, 2006.

[60] Prodanovic, M and Bryant, S. L. Physics-driven interface modeling for drainage and imbibition in fractures. *SPE Journal*, 14(03):532–542, 2009.

[61] Shabro, V, Prodanovic, M, Arns, C. H, Bryant, S. L, Torres-Verdin, C, and Knackstedt, M. A. Pore-scale modeling of two-phase flow. In *XVIII International Conference on Computational Methods in Water Resources, Barcelona*, 2010.

[62] Rodriguez, E, Prodanović, M, and Bryant, S. L. Contact line extraction and length measurements in model sediments and sedimentary rocks. *Journal of Colloid and Interface Science*, 368(1):558 – 577, 2012.

[63] Strikwerda, J. C. *Finite difference schemes and partial differential equations*. Siam, 2004.

[64] Aster, R. C, Borchers, B, and Thurber, C. H. *Parameter estimation and inverse problems*. Academic Press, 2013.

[65] Saad, Y. *Iterative methods for sparse linear systems*. Siam, 2003.

[66] Van der Vorst, H. A. Bi-cgstab: A fast and smoothly converging variant of bi-cg for the solution of nonsymmetric linear systems. *SIAM Journal on scientific and Statistical Computing*, 13(2):631–644, 1992.

[67] Kumar, M. *Multiphase flow in reservoir cores using digital core analysis*. Australian National University, 2009.

[68] Mousavi, M. A and Bryant, S. L. Geometric models of porosity reduction mechanisms in tight gas sands. In *Rocky Mountain Oil & Gas Technology Symposium*. Society of Petroleum Engineers, 2007.

[69] Prodanović, M, Bryant, S. L, and Davis, J. S. Numerical simulation of diagenetic alteration and its effect on residual gas in tight gas sandstones. *Transport in Porous Media*, 96(1):39–62, 2013.

[70] Nock, R and Nielsen, F. Statistical region merging. *Pattern Analysis and Machine Intelligence, IEEE Transactions on*, 26(11):1452–1458, 2004.

[71] Sen, P, Scala, C, and Cohen, M. A self-similar model for sedimentary rocks with application to the dielectric constant of fused glass beads. *Geophysics*, 46(5):781–795, 1981.

[72] Mendelson, K. S and Cohen, M. H. The effect of grain anisotropy on the electrical properties of sedimentary rocks. *Geophysics*, 47(2):257–263, 1982.

[73] Doyen, P. M. Permeability, conductivity, and pore geometry of sandstone. *Journal of Geophysical Research: Solid Earth (1978–2012)*, 93(B7):7729–7740, 1988.

[74] Ehrlich, R. Viscous coupling in two-phase flow in porous media and its effect on relative permeabilities. *Transport in Porous Media*, 11(3):201–218, 1993.